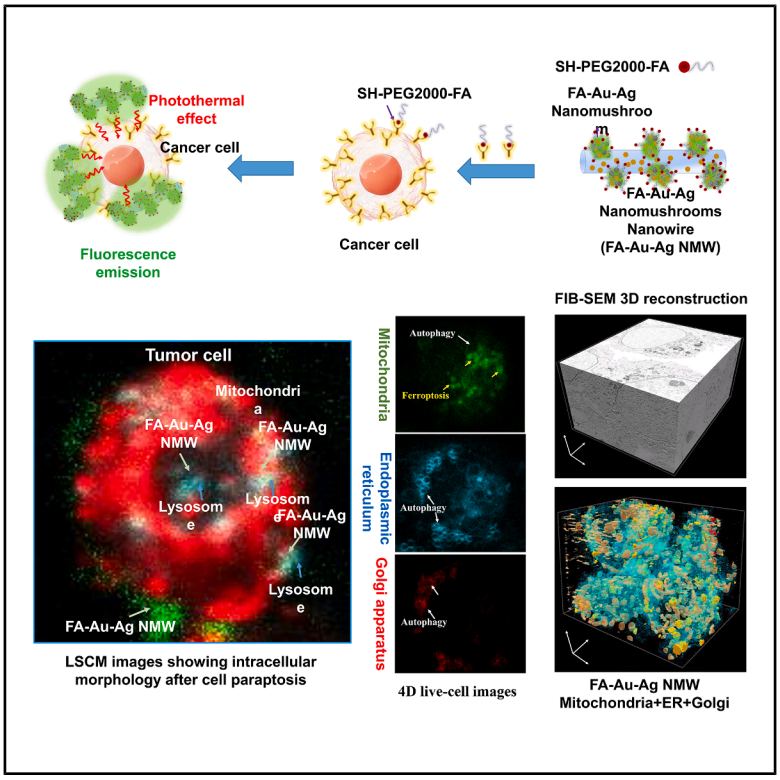
Cell Reports
Physical Science

Article

Photon-driven alloy nanostructures trigger paraptosis through organelle disruption

Graphical abstract



Highlights

- Self-assembled FA-Au-Ag nanomushroom-nanowires respond to light
- Light triggers ER stress and calcium dyshomeostasis
- Multi-organelle vacuolization accompanies caspase-independent paraptosis
- 4D live-cell imaging and FIB-SEM 3D reconstruction visualize paraptotic changes

Authors

Haojian Qiu, Hailang Dai, Yujie Qi, Yi Lai, Xianfeng Chen

Correspondence

hailangdai@sjtu.edu.cn (H.D.), xfchen@sjtu.edu.cn (X.C.)

In brief

Qiu et al. report FA-Au-Ag alloy nanostructures for fluorescence-guided phototherapy. These nanostructures trigger ER stress, calcium imbalance, and multi-organelle vacuolization to induce paraptosis and overcome tumor compensation.

Qiu et al., 2026, Cell Reports Physical Science 7, 103652
November 18, 2026 © 2026 The Author(s). Published by Elsevier Inc.
https://doi.org/10.1016/j.xcrp.2026.103652

CellPress

Cell Reports
Physical Science

CellPress
OPEN ACCESS

Article

Photon-driven alloy nanostructures trigger paraptosis through organelle disruption

Haojian Qiu,[1,4] Hailang Dai,[1,4,5,*] Yujie Qi,[1,4] Yi Lai,[2] and Xianfeng Chen[1,3,*]
[1]School of Physics and Astronomy, Shanghai Jiao Tong University, Shanghai 200240, China
[2]Department of Head and Neck Surgery, Department of Traditional Chinese Medicine, Renji Hospital, Shanghai Jiao Tong University School of Medicine, Shanghai 200240, China
[3]Collaborative Innovation Center of Light Manipulations and Applications, Shandong Normal University, Jinan 250358, China
[4]These authors contributed equally
[5]Lead contact
*Correspondence: hailangdai@sjtu.edu.cn (H.D.), xfchen@sjtu.edu.cn (X.C.)
https://doi.org/10.1016/j.xcrp.2026.103652

SUMMARY

Many organelle-targeted anticancer strategies are designed primarily to perturb a specific organelle, potentially allowing tumor cells to activate compensatory responses that limit therapeutic efficacy. Paraptosis, a non-apoptotic programmed cell death characterized by multi-organelle vacuolization, provides an alternative strategy to bypass apoptosis resistance. Here, we report a photon-driven therapeutic platform based on self-assembled FA-Au-Ag alloy nanomushroom-nanowires for fluorescence-guided induction of paraptosis in tumor cells. Equipped with folate targeting and plasmonic properties, the nanostructures enable precise intracellular translocation under light irradiation. Combined with 4D live-cell imaging and FIB-SEM 3D reconstruction, we show that the photoresponsive nanosystem triggers endoplasmic reticulum stress and calcium dyshomeostasis. Such cascade responses further disrupt mitochondrial redox balance, causing synchronous foaming of multiple organelles to initiate caspase-independent paraptosis. This multi-organelle destructive pattern efficiently abrogates tumor compensatory capability. This work develops a multifunctional alloy nanoplatform, offering great potential for fluorescence-guided phototherapy.

INTRODUCTION

Cell apoptosis is typically triggered by functional anomalies or structural impairment of intracellular organelles, making the selective disruption of organelles a pivotal focus for rational therapeutic design in oncology and other disease areas.[1–3] In cancer treatment, the pursuit of effective and durable antitumor efficacy has driven extensive exploration of organelle-targeted strategies, as tumor cells exhibit distinct subcellular characteristics that distinguish them from normal cells.[4–6] Specifically, tumor cells are characterized by hyperactive metabolic profiles to support their uncontrolled proliferation, accompanied by significantly elevated mitochondrial abundance, a hallmark metabolic adaptation that has rendered mitochondria a long-standing research hotspot for antitumor interventions in the burgeoning field of nanomedicine.[7–9] Over the past decade, various nanocarriers and nanotherapeutics have been developed to target mitochondria, leveraging their unique metabolic role to induce tumor cell death.

However, an increasing body of evidence indicates that cellular metabolism is not a simplistic, isolated process confined to mitochondrial ATP biosynthesis.[10–12] Instead, it relies on the intricate synergistic interplay of multiple organelles, including mitochondria, endoplasmic reticulum (ER), and Golgi apparatus. Mitochondria supply energy for cellular activities, the ER regulates protein folding and calcium homeostasis, and the Golgi apparatus is responsible for protein modification and trafficking; these organelles communicate dynamically through complex signaling cascades to maintain cellular homeostasis and support tumor progression.[13–15] This interconnected organelle network underscores a major caveat of canonical mitochondria-directed therapeutics: strategies exclusively aimed at abrogating mitochondrial function are insufficient to disrupt the wider metabolic and regulatory circuitry of tumor cells. Although mitochondrial stress can drive apoptotic cell death, metabolic plasticity or blunted activation of the mitochondrial apoptotic cascade in particular tumor microenvironments frequently curtails treatment response, yielding incomplete and transient antitumor activity.[16]

The root cause of this shortcoming lies in the hallmark capacity of cancer cells for functional compensation and damage repair. Cancer cells possess robust adaptive mechanisms to circumvent single-organelle dysfunction, for instance, they can upregulate alternative metabolic pathways or enhance organelle biogenesis to offset mitochondrial impairment.[16] This adaptive response not only limits the efficacy of single-target therapies but also drives the emergence of chemoresistance, a major clinical challenge that severely hinders the long-term success of cancer treatment. Chemoresistance accounts for over 90% of

This is an open access article under the CC BY-NC-ND license (http://creativecommons.org/licenses/by-nc-nd/4.0/).

treatment failure in advanced cancers,[17] highlighting the urgent need to develop innovative therapeutic platforms that can bypass single-organelle targeting limitations and induce multi-organelle dysfunction to eliminate tumor cells more comprehensively and irreversibly.

Nanomedicine has emerged as a transformative field to address these challenges, offering unparalleled advantages in targeted delivery, controlled drug release, and multimodal therapy integration.[18–20] Multifunctional nanostructures, in particular, have gained significant attention due to their ability to integrate targeting, therapeutic, and imaging functionalities into a single platform. Among these, noble metal nanostructures (e.g., Au and Ag alloys) have shown great potential for phototherapies, as they can generate localized surface plasmon resonance (LSPR) upon photon irradiation—an effect that enables efficient membrane disruption, photothermal therapy, or reactive oxygen species (ROS) generation.[21,22] Additionally, surface modification with targeting ligands such as folic acid (FA) allows for selective accumulation in tumor cells overexpressing folate receptors (FRs), minimizing off-target cytotoxicity and enhancing therapeutic precision.[23,24]

Here, we report a photon-assisted therapeutic platform based on self-assembled, folate-modified Au-Ag alloy nanomushroom-nanowires (FA-Au-Ag NMWs). Upon light irradiation, the nanostructures mediate cell membrane disruption and intracellular translocation and trigger ER stress and calcium dyshomeostasis. These responses are associated with multi-organelle vacuolization and caspase-independent paraptosis. Four-dimensional live-cell imaging and focused ion beam scanning electron microscope (FIB-SEM) three-dimensional (3D) reconstruction visualize the associated subcellular changes. The platform integrates fluorescence tracking and phototherapeutic activity, providing an approach to inducing paraptosis through multi-organelle perturbation.

RESULTS AND DISCUSSION

Rapid transmembrane translocation of folate-modified alloy nanostructures under light irradiation

Rational design of plasmonic nanostructures with tailored architecture and targeting capability is pivotal for advancing photon-driven nanotherapeutics, as it enables precise control over intracellular delivery, subcellular localization, and therapeutic response while mitigating off-target toxicity. Here, we report folate receptor (FOLR1)-targeted Au-Ag nanomushroom-nanowires (FA-Au-Ag NMWs) engineered to leverage LSPR-mediated photon responsiveness for tumor-selective internalization and subsequent cell death induction. Figure 1 systematically delineates the synthesis, dynamic growth, targeting specificity, photon-driven membrane interaction, and intracellular distribution of FA-Au-Ag NMWs, providing direct experimental evidence for their utility as next-generation plasmonic nanocarriers for ovarian cancer (A2780) therapy. The hierarchical FA-Au-Ag NMW architecture was fabricated via a controlled stepwise synthesis, with its growth process dynamically monitored using *in situ* transmission electron microscopy (TEM) to ensure structural fidelity (Figure 1B and supplemental methods, section I). As highlighted by arrows in Figure 1B, distinct nanomushroom growth domains were clearly resolved, demonstrating the controlled nucleation and growth of Au-Ag nanomushroom caps on the nanowire backbone. This hierarchical structure—combining a one-dimensional (1D) nanowire for enhanced cellular penetration and 3D nanomushroom caps for optimized LSPR and ligand conjugation—was rationally designed to integrate structural advantages for both targeting and photon responsiveness. Meanwhile, scanning electron microscopy (SEM) characterization was employed to verify the successful conjugation of FA onto the Au-Ag NMW surface (Figure 1C). FA functionalization is essential for FOLR1-mediated active targeting, as FOLR1 is overexpressed in A2780 ovarian cancer cells but minimally expressed in normal cells, enabling tumor-selective recognition. SEM micrographs of FA-conjugated NMWs revealed a uniform surface modification compared to unfunctionalized Au-Ag NMWs (section I of the supplemental information), with no observable aggregation—indicating stable FA anchoring and preserved nanostructural integrity. This structural uniformity is critical for consistent plasmonic performance and targeting efficiency, as aggregation would compromise LSPR activity and increase nonspecific cellular interactions.

The targeting specificity of FA-Au-Ag NMWs toward A2780 tumor cells was validated using cryo-electron microscopy (cryo-EM) mapping, which provides high-resolution visualization of nanostructure-cell interactions in near-native conditions (Figure 1D). Cryo-EM circumvents artifacts associated with conventional fixation methods, ensuring accurate assessment of NMW localization. As shown in Figure 1D, FA-Au-Ag NMWs were specifically localized on and in the vicinity of A2780 cell, with minimal nonspecific binding-confirming efficient FOLR1-mediated recognition. In contrast, unfunctionalized Au-Ag NMWs exhibited negligible association with A2780 cells (section X of the supplemental information), further corroborating that FA conjugation is indispensable for tumor-selective targeting.

Photon stimulation (LED irradiation) was employed to trigger membrane perforation, a key step for enhancing FA-Au-Ag NMW internalization, with cryo-EM combined with FIB milling used to resolve membrane changes at the nanoscale (Figure 1E). White dashed circles in Figure 1E highlight membrane pores induced by FA-Au-Ag NMWs under LED irradiation, with pore formation attributed to LSPR-mediated photothermal conversion: the nanomushroom caps efficiently absorb photon energy and convert it to localized heat, inducing transient membrane disruption. This photothermal effect is highly localized to the FA-Au-Ag NMW-membrane interface, minimizing collateral damage to surrounding normal cells, a critical feature for safe therapeutic applications.

Quantitative analysis of membrane pore area (Figure 1F) demonstrated a positive correlation with LED irradiation duration, with pore size increasing as irradiation time extended. This time-dependent membrane disruption reflects the cumulative effect of photothermal heating, as prolonged irradiation enhances local temperature elevation and subsequent membrane fluidity and perforation. To confirm that membrane perforation was associated with functional damage, lactate dehydrogenase (LDH) release was quantified using a fluorometric assay (Figure 1G). LDH is a cytosolic enzyme released upon membrane disruption, serving as a reliable marker of membrane integrity.

CellPress
OPEN ACCESS

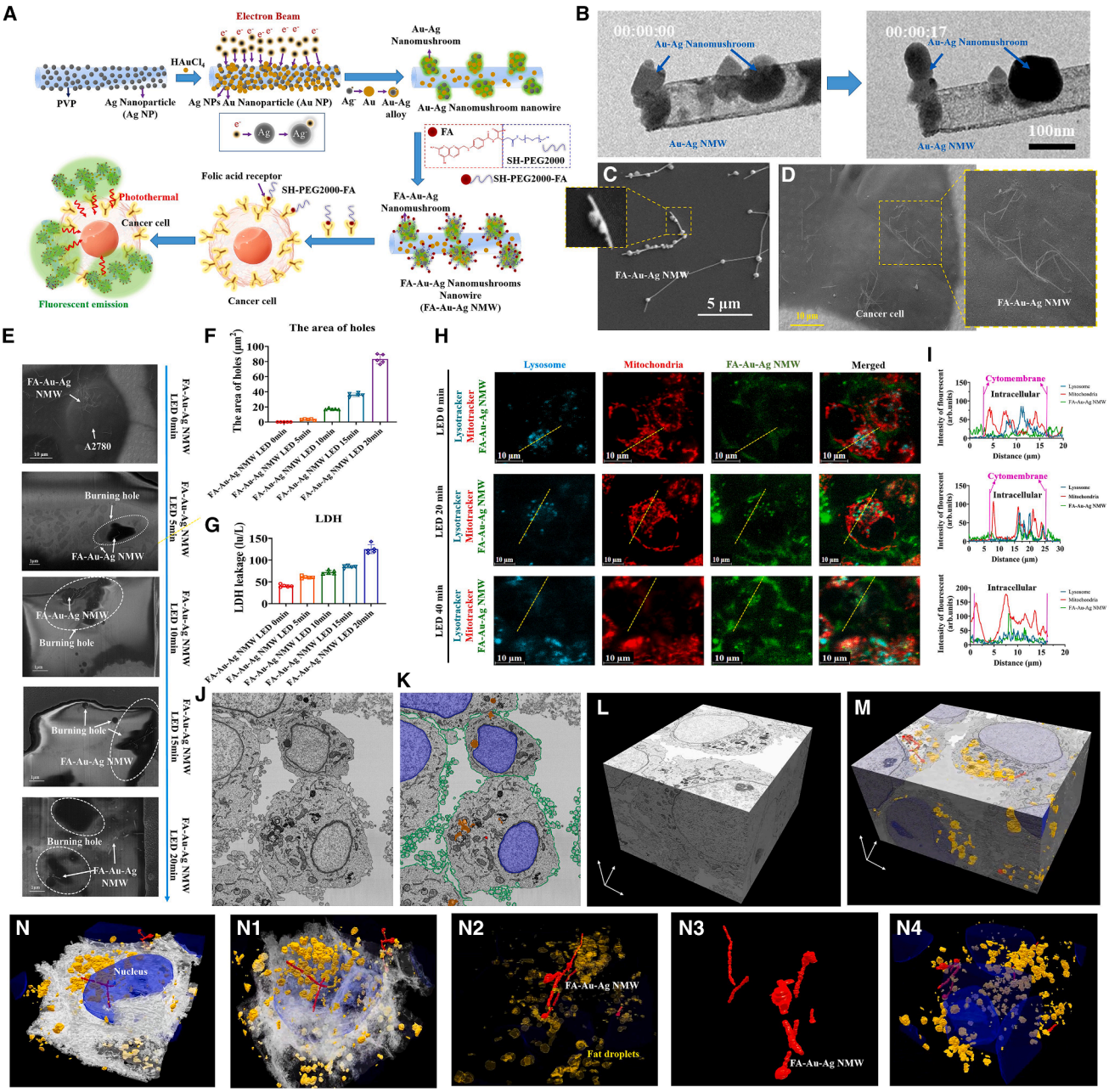


Figure 1. Synthesis, characterization, and photon-driven internalization of FA-Au-Ag nanomushroom-nanowires

(A) Synthetic schematic of FA-Au-Ag nanostructures.

(B) *In situ* STEM observation of nanomushroom growth (blue arrows).

(C) SEM image of FA-modified nanocomposites.

(D) Cryo-EM mapping of intracellular nanomaterial distribution in A2780 cells.

(E) FIB-cryo-EM images showing time-dependent membrane perforation under LED irradiation (white dashed circles).

(F) Quantitative statistics of membrane pore area.

(G) Fluorometric quantification of LDH release (n = 5).

(H and I) LSCM co-localization and quantitative analysis of nanomaterial subcellular distribution.

(J–N4) FIB-SEM intracellular observation and deep learning-based 3D reconstruction of cellular ultrastructures (Video S1).

Quantitative summary data are presented as mean ± SD. Scale bars: 100 nm in (B, right image), 5 μm in (C, main image), 10 μm in (D, main image; E, 0 min; H), and 1 μm in (E, 5–20 min). See also Figures S1–S5 and Video S1.

Significantly increased LDH release was observed in the FA-Au-Ag NMW + LED irradiation group compared to control groups (no irradiation, unfunctionalized NMWs), confirming that photon-driven membrane perforation is functionally relevant and contributes to cellular dysfunction—a prerequisite for subsequent cell death induction.

Moreover, laser scanning confocal microscopy (LSCM) and fluorescence co-localization were used to investigate the intracellular distribution of FA-Au-Ag NMWs under different light conditions (Figure 1H), with lysosomes (cyan) and mitochondria (red) labeled to assess subcellular targeting. Co-localization analysis is critical for understanding FA-Au-Ag NMW trafficking and potential subcellular therapeutic targets, as mitochondria and lysosomes are key organelles involved in cell death pathways (apoptosis and paraptosis) and intracellular degradation, respectively. Figure 1H shows distinct co-localization of FA-Au-Ag NMWs (green) with both lysosomes and mitochondria, indicating that photon-driven internalization leads to FA-Au-Ag NMW accumulation in these organelles. This dual subcellular localization suggests that FA-Au-Ag NMWs may target multiple cell death pathways simultaneously, enhancing therapeutic efficacy. To quantify FA-Au-Ag NMW distribution across different cellular compartments, fluorescence co-localization analysis of signal intensity inside, outside, and on the cell membrane was performed (Figure 1I). This quantitative assessment confirmed that photon irradiation significantly increased intracellular FA-Au-Ag NMW accumulation, with the majority of FA-Au-Ag NMWs localized inside the cell or associated with the membrane after irradiation. In contrast, minimal intracellular accumulation was observed in the absence of irradiation, highlighting the critical role of photon stimulation in promoting FA-Au-Ag NMW internalization. This photon-dependent internalization is a key advantage of FA-Au-Ag NMWs, as it enables spatiotemporal control over delivery only activating internalization in tumor regions exposed to light, further enhancing tumor specificity.

Deep learning-assisted 3D reconstruction of FIB-SEM slices was employed to visualize the detailed intracellular localization of FA-Au-Ag NMWs relative to key subcellular structures (Figures 1J-n4 and supplemental methods, section XI). Deep learning enhances the segmentation of FIB-cryo-EM data, enabling precise mapping of NMWs (red) relative to the nucleus (purple), cell membrane (green), lipid droplets (yellow), and cellular protein filaments (white). Figure 1J shows a representative FIB-cryo-EM slice of A2780 cells after treatment with FA-Au-Ag NMWs + LED irradiation, with detailed segmentation of organelles and NMWs in Figures 1K-n4. 3D reconstruction (Figures 1K-n4) further confirmed that FA-Au-Ag NMWs accumulate in the cytoplasm, with preferential localization near mitochondria and the ER-consistent with LSCM co-localization results. This subcellular distribution is strategically advantageous, as targeting mitochondria and ER enables direct induction of organelle dysfunction, a potent driver of tumor cell death.

The results from Figure 1 collectively demonstrate that FA-Au-Ag NMWs possess three key features critical for advanced nanotherapeutics: (1) controlled hierarchical structure with optimized plasmonic properties, validated via *in situ* TEM and SEM; (2) FOLR1-mediated tumor selectivity, confirmed by cryo-EM mapping; (3) photon-driven membrane perforation and intracellular delivery, supported by FIB-SEM, LDH release, and confocal imaging. These features address major challenges in nanotherapeutics, including poor targeting specificity, limited intracellular delivery, and lack of spatiotemporal control. Notably, the combination of FA targeting and photon-driven internalization enables a ''double-selectivity'' strategy: tumor cells are first targeted via FOLR1-FA interaction, and internalization is only activated via photon irradiation-minimizing off-target effects even in tissues with low FOLR1 expression. Additionally, the hierarchical nanomushroom-nanowire architecture optimizes LSPR activity, ensuring efficient photothermal conversion and membrane perforation at clinically relevant light intensities, which is critical for translational potential. Thus, Figure 1 provides comprehensive experimental evidence for the rational design and functional utility of FA-Au-Ag NMWs as photon-responsive, tumor-targeted nanocarriers. The structural characterization, targeting specificity, and photon-driven internalization demonstrated here lay the foundation for subsequent investigations into organelle dysfunction (Figure 2).

Targeting specificity and optical and plasmonic electrical properties of alloy nanostructures

For photon-nanotherapeutics, robust targeting capability and tailored optical/electrical properties are indispensable for translating structural design into therapeutic efficacy. Figure 2 systematically validates the FOLR1-mediated targeting specificity, fluorescence emission, LSPR, and electrical conductivity of FA-Au-Ag NMWs-key functionalities that synergize to enable precise tumor targeting and photon-driven therapeutic responses.

Folate conjugation and FOLR1 targeting were corroborated via complementary spectroscopic and cellular assays. TEM and elemental mapping (Figure 2B) confirmed the uniform distribution of Au, Ag, and C/O (from FA) in FA-Au-Ag NMWs, verifying successful ligand anchoring. X-ray photoelectron spectroscopy (XPS) further validated FA conjugation: the linkage between SH-PEG2000-FA and AuNPs is mediated through O-C=O bonds, as evidenced by both XPS and Fourier transform infrared (FTIR) analyses. FA-Au-Ag NMWs (Figures 2C1-c3) exhibited enhanced C1s and O1s signals compared to unfunctionalized Au-Ag NMWs (Figures 2C4-c6), consistent with FA's carbon-rich and oxygen-rich molecular structure, comparative analysis of the C and O functional groups between bare Au-Ag NMW and FA-Au-Ag NMW confirmed the emergence of O–C=O bonds in the latter. FTIR spectra further revealed a distinct transmission peak centered at 1,684 cm^{-1} for FA-Au-Ag NMW, which is illustrated in Figure 2D. By comparing the spectra of phosphate-buffered saline (PBS), bare Au-Ag NPs-NW, and free FA molecules, we verified that FA molecules are covalently conjugated to Au-Ag NPs-NWs via O-C=O bonds, corresponding to the characteristic peak at 1,684 cm^{-1}.

The optical and LSPR properties of FA-Au-Ag NMWs were optimized for photon absorption and photothermal conversion. COMSOL simulations (Figures 2F and 2G) demonstrated superior electromagnetic field distribution in the nanomushroom region under broadband (400–1,100 nm) irradiation, with photothermal efficiency positively correlated with nanomushroom density-consistent with Figure 1 photothermal membrane

CellPress
OPEN ACCESS

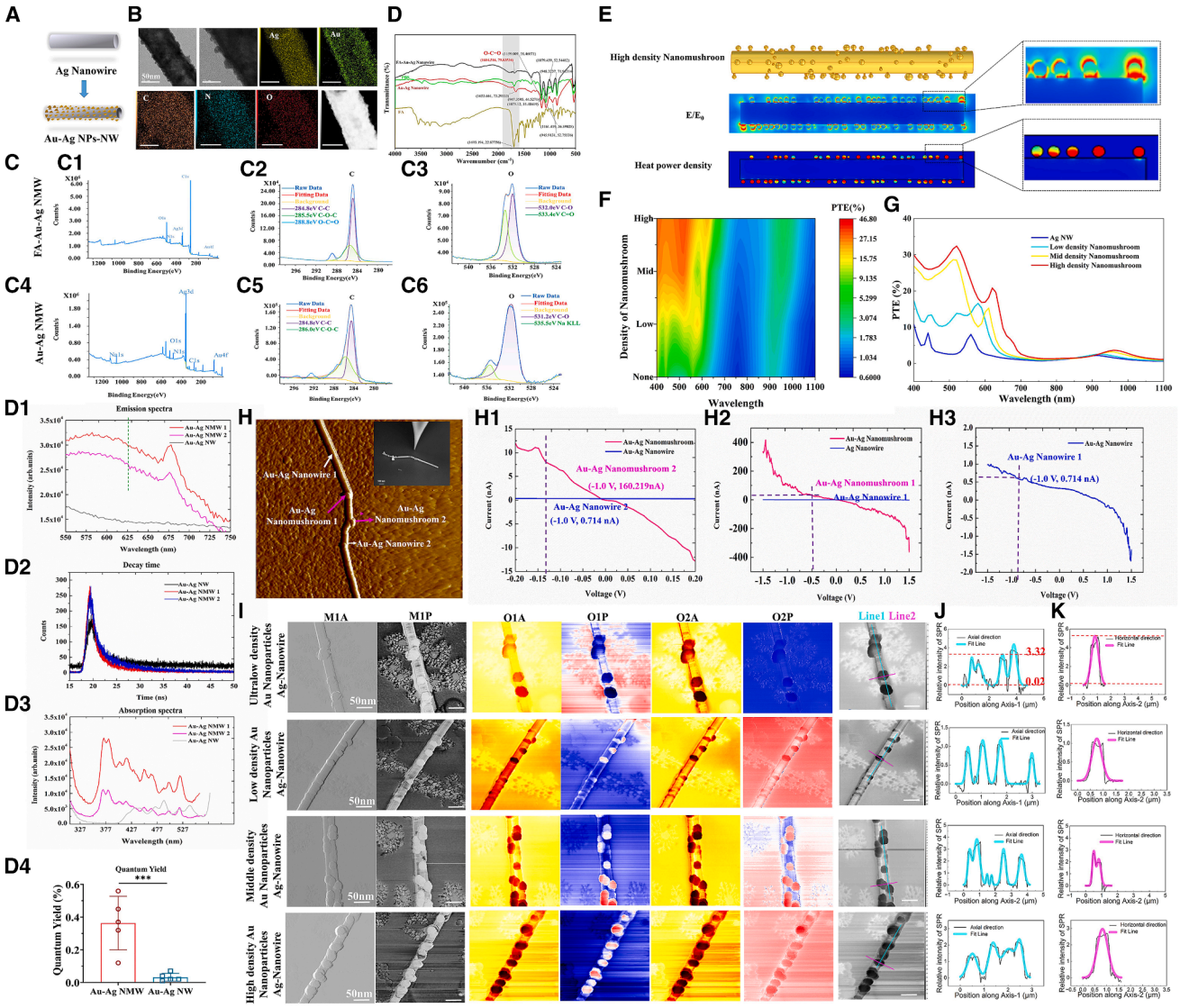


Figure 2. Targeting, optical, plasmonic, and electrical properties of FA-Au-Ag NMW

(A) Schematic of FA-Au-Ag NMW cell membrane targeting.

(B) TEM image and elemental mapping of FA-Au-Ag NMW.

(C–C6) XPS survey and high-resolution C1s/O1s spectra of FA-Au-Ag NMW and pristine Au-Ag NMW for verifying FA conjugation.

(D–D4) FTIR spectra of free FA, Au-Ag NMW, FA-Au-Ag NMW, and PBS (D). (D1–D4) Fluorescence emission, lifetime, absorption, and quantum yield of Au-Ag NMW.

(E–G) COMSOL simulations of electromagnetic field distribution and photothermal performance of Au-Ag NMW under broadband irradiation at varied nanomushroom densities.

(H–H3) AFM-based spatially resolved C-V measurements of FA-Au-Ag NMW nanomushrooms and nanowires.

(I–K) NanoIR-AFM characterization of localized LSPR and photothermal conversion across nanostructural regions. Scale bars: 50 nm in (B, first TEM image), 20 nm in (B, second TEM image), 300 nm in (H, inset), and 50 nm in (I, M1A images). Error bars in (D4) represent SD. See also sections I–IV and VIII of the supplemental information and Figures S6–S17, S29, and S30.

perforation data. This density-dependent plasmonic performance enables tunable photothermal responses to diverse therapeutic scenarios. Systematic optical characterization (Figures 2D1-d4) revealed favorable emission spectra, normal fluorescence lifetime, strong broadband absorption, and acceptable quantum yield for Au-Ag NMWs-properties that support both fluorescence imaging and photon energy conversion. Analysis of the emission spectra revealed that Au-Ag NMW exhibits a distinct fluorescence peak at 550–600 nm, with a full width at half maximum (FWHM) of approximately 50 nm. Furthermore, the fluorescence intensity was found to be positively correlated with the nanomushroom density: the denser nanostructure (Au-Ag NMW2) displayed a higher fluorescence peak intensity than the less dense counterpart (Au-Ag NMW1).

Notably, no fluorescence signal was detected for the mushroom cap-free Au-Ag nanowires. The fluorescence decay time of Au-Ag NMW was measured to characterize its excited-state dynamics. As shown in the figure, the decay curves of Au-Ag NMW and Au-Ag nanowires were well fitted with a bi-exponential decay model, yielding average decay times of τ_1 = 7.6 ns (Au-Ag NMW) and τ_2 = 1.7 ns (the mushroom cap-free Au-Ag nanowires), respectively. Complementary absorption spectra measurements further characterized the optical absorption properties of the two nanostructures. Across the excitation wavelength range of 250–550 nm, Au-Ag NMW exhibited a higher overall absorption efficiency than the mushroom cap-free Au-Ag nanowires. Specifically, in the ultraviolet region (<300 nm), the imaginary part of silver's dielectric constant assumes a positive value, which diminishes its metallic characteristics and consequently gives rise to a prominent absorption peak in this range. We also determined the quantum yields of both nanostructures under 350 nm excitation. Experimental results demonstrated that Au-Ag NMW achieved a quantum yield of 0.37%, whereas the mushroom cap-free Au-Ag nanowires exhibited a negligible quantum yield of only 0.07%, which is close to zero. This finding is consistent with our emission spectroscopy data, as the mushroom cap-free Au-Ag nanowires showed almost no fluorescence emission.

Atomic force microscopy (AFM)-based C-V curves (Figures 2H-h3) demonstrated excellent electrical conductivity of FA-Au-Ag NMWs, with distinct responses between nanomushroom and nanowire domains when swept from −1.5 to 1.5 V (0.1 V step), and the conductivity has increased by more than two orders of magnitude compared to the Au-Ag nanowire without the growth of nanomushroom. This conductivity, coupled with LSPR, enables plasmonic-electrical synergy: photon-induced plasmonic excitation enhances charge carrier mobility, potentially amplifying photothermal effects and membrane disruption-complementing Figure 1's photon-driven internalization data. Therefore, we employed nanoscale infrared spectroscopy coupled with AFM (AFM-IR) to directly characterize the photothermal conversion behavior of the nanomushroom structures in Au-Ag NMWs and their adjacent regions (Figure 2I). By mapping the electric field density distribution, we were able to indirectly evaluate the conversion efficiency of incident light at the nanomushroom sites. Specifically, upon resonant coupling with electrons in the nanostructures, incident light is confined into high-density localized fields, with the majority of its energy converted into thermal energy. In this study, we systematically compared the localized field densities between regions decorated with nanomushrooms and those devoid of nanomushrooms on Au-Ag NMWs. The results revealed that the localized field intensity at the nanomushroom sites was over 200-fold higher than that at the non-decorated regions (Figure 2J). These experiments further confirmed that localized photothermal conversion is confined to the nanomushroom domains (with an area of approximately tens of square nanometers), which can be approximated as nanoscale point sources generating localized high-temperature regions. In contrast, the photothermal conversion efficiency and temperature values measured for the entire Au-Ag NMW nanostructures represent only the macroscopic average of the overall thermal effect, rather than the localized thermal response at the nanomushroom sites.

In Figure 3, cellular targeting assays confirmed FOLR1-mediated selectivity (Figure 3A). LSCM fluorescence mapping (Figure 3B) confirmed intense green fluorescence of FA-Au-Ag NMWs in A2780 cells under 473 nm laser excitation (10 mW), validating their potential for real-time imaging-guided therapy. LSCM imaging (Figure 3B) showed intense green fluorescence (FA-Au-Ag NMWs) on A2780 cells, while normal cells exhibited minimal signal—reflecting FOLR1 overexpression in tumor cells. Pre-incubation with free FA or FOLR1 silencing via siRNA significantly reduced fluorescence intensity (Figure 3E), confirming FA-FOLR1 interaction-dependent targeting. qPCR analysis (Figure 3G) identified the most effective FOLR1(h)-siRNA, which robustly downregulated FOLR1 expression, further validating targeting specificity. Competitive binding assays (Figures 3C and 3D) reinforced these findings, with excess free FA abrogating NMW binding to A2780 cells, critical for minimizing off-target accumulation in normal tissues.

Thus, Figures 2 and 3 findings synergize with Figure 1 to establish FA-Au-Ag NMWs' multifunctional potential: FOLR1 targeting ensures tumor selectivity, optimized LSPR and optical properties enable efficient photon energy conversion, and electrical conductivity enhances plasmonic responses. The multimodal validation of FA conjugation (XPS, FTIR, TEM) and targeting (cellular assays, siRNA silencing) confirms reproducible and specific tumor recognition, while plasmonic-electrical-optical integration supports both imaging and therapy. These properties address critical bottlenecks in nanotherapeutics, including poor targeting precision and inefficient photon-to-therapeutic effect conversion. Collectively, Figures 2 and 3 validates FA-Au-Ag NMWs as a well-engineered plasmonic platform, laying the groundwork for investigating their organelle-targeting effects and molecular mechanisms of cell death.

Subcellular visualization by 4D live cell imaging and deep learning-assisted 3D reconstruction

Organelle homeostasis is pivotal for cell survival, and targeted disruption of key organelles (mitochondria, ER, and Golgi apparatus) represents a potent strategy for tumor therapy. Figure 4 employs 4D live-cell imaging, organelle staining, and deep learning-assisted SEM analysis to systematically characterize FA-Au-Ag NMW-induced organelle dynamics under photon stimulation, bridging nanostructure internalization (Figure 1) and functional properties (Figure 2) to elucidate early-stage therapeutic mechanisms in A2780 cells.

LSCM imaging, live/dead staining, and CCK-8 measurements were used to examine the cellular response to FA-Au-Ag NMW treatment under photon irradiation. Before irradiation, A2780 cells showed no obvious morphological abnormalities (Figure 4A). After 40 min of irradiation, live/dead staining showed increased red fluorescence and decreased green fluorescence (Figure 4B). The CCK-8/WST-8 reduction signal was also reduced following the combined treatment (Figure 4C). Together with the membrane perforation observed in Figure 1, these observations are consistent with treatment-associated cellular injury. The CCK-8 results are interpreted as changes in WST-8 reduction under the assay conditions rather than as direct

CellPress
OPEN ACCESS

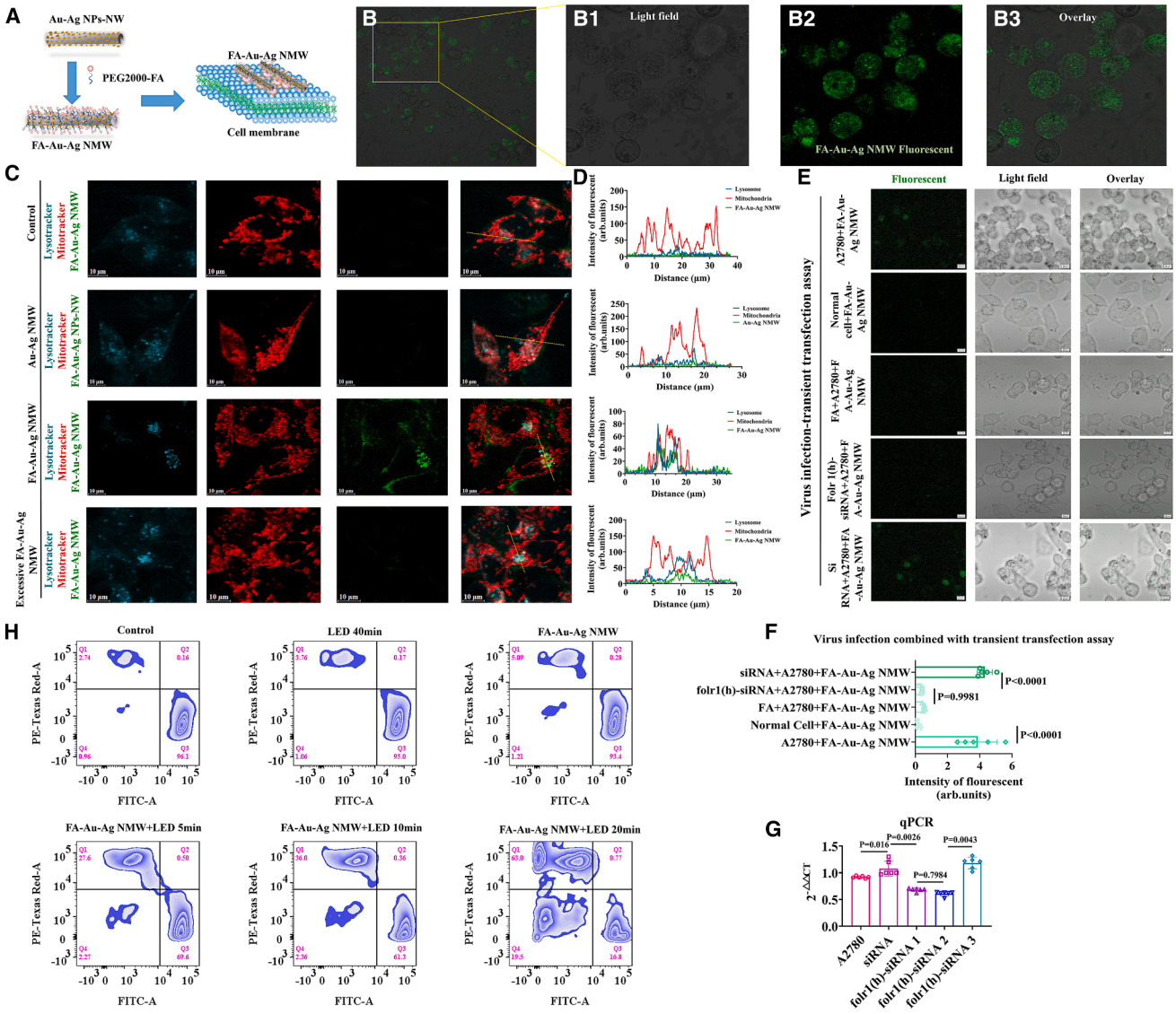


Figure 3. Validation of the targeting capability of FA-Au-Ag NMW

(A) Schematic illustration of FA-Au-Ag NMW targeting tumor cells.

(B–B3) LSCM fluorescence distribution of target-adsorbed FA-Au-Ag NMW on tumor cell surfaces.

(C) LSCM fluorescence mapping of intracellular FA-Au-Ag NMW in A2780 cells under 473 nm laser excitation.

(D) LSCM co-localization analysis of competitive folate binding assay with four experimental groups.

(E) LSCM observation of cellular uptake after FOLR1 gene silencing via siRNA interference in multiple cell treatment groups.

(F) Quantitative fluorescence intensity analysis of nanomaterials around and on cell membranes (n = 5).

(G) qPCR quantification of FR expression under different RNA interference conditions (n = 5).

(H) Live/dead staining of ovarian cancer cells under diverse treatments.

Quantitative summary data are presented as mean ± SD. Scale bars: 10 μm in (C) and 20 μm in (E). See also Figures S19–S23 and S31.

measurements of cell death or colony-forming capacity. To complement the CCK-8 measurements, a clonogenic assay was performed in A2780 cells. Representative images and descriptive quantification of crystal violet-stained area showed less colony-associated staining in the NMW + light group than in the control, NMW, and light groups, consistent with reduced colony outgrowth under the tested conditions (supplemental material, section XV; Figure S41; Table S1).

Organelle-specific fluorescent staining revealed distinct morphological changes between control and experimental groups. Cells treated with photon irradiation alone (Figure 4D) retained intact mitochondria (green), ER (cyan), and Golgi apparatus (red), with normal spatial distribution. In contrast, co-treatment with FA-Au-Ag NMWs and photon irradiation (Figure 4E) caused severe fragmentation of mitochondria, ER expansion and disassembly, and Golgi apparatus collapse—indicating

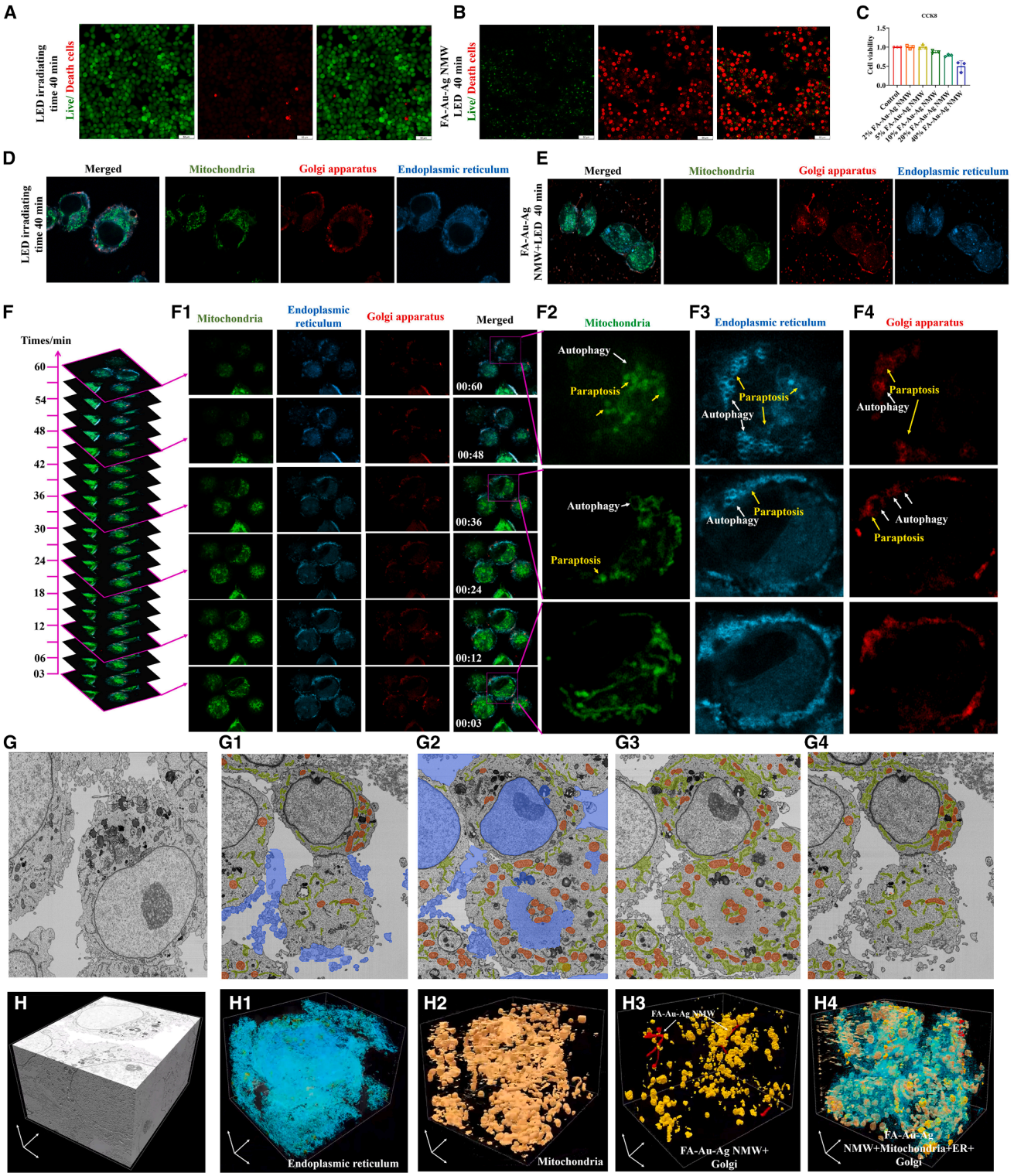


Figure 4. 4D monitoring of organelle dynamics in photon-stimulated A2780 cells with FA-Au-Ag NMW treatment

(A–C) LSCM imaging, live/dead staining, and CCK-8 measurements of cellular responses to photon irradiation in FA-Au-Ag NMW-treated A2780 cells.

(A) Cell state before irradiation.

(B) Live/dead staining after 40 min irradiation (green: live cells; red: dead cells).

(C) CCK-8 reduction signal.

(legend continued on next page)

that NMW-mediated plasmonic effects specifically disrupt organelle integrity, rather than non-specific photon damage. 4D live-cell imaging (captured at 2-min intervals over 60 min; Figures 4F-f4) dynamically tracked time-dependent organelle dysfunction. Representative image sequences (Figure 4F) and morphological analysis (Figure 4F1) showed progressive deterioration: mitochondria (Figure 4F2) underwent gradual fragmentation, ER (Figure 4F3) expanded and lost structural continuity, and the Golgi apparatus (Figure 4F4) disassembled over time. This temporal progression correlates with photon-driven NMW internalization and plasmonic heating, suggesting that organelle damage is a sequential process initiated by membrane disruption and amplified by subcellular NMW accumulation (supplemental methods, section XII).

Deep learning-assisted segmentation of FIB-SEM slices (Figure 4G-g4) and 3D reconstruction (Figures 4H-h4) resolved the spatial relationship between FA-Au-Ag NMWs and organelles. Segmentation clearly distinguished mitochondria, ER, Golgi apparatus, nucleus, cell membrane, and NMWs (Figures 4g1-g4), while 3D models confirmed FA-Au-Ag NMWs (red) accumulate preferentially near mitochondria (orange) and ER (cyan) (Figures 4h1–h4). This proximity explains the targeted organelle damage observed, as localized plasmonic heating from adjacent NMWs directly impairs organelle function—validating the design rationale of leveraging subcellular localization for enhanced therapeutic efficacy (supplemental methods, section XI; Video S2).

Figure 4 findings integrate with prior data to clarify FA-Au-Ag NMW therapeutic mechanisms: photon-driven internalization (Figure 1) and plasmonic activity (Figure 2) enable targeted organelle disruption, with 4D imaging confirming sequential dysfunction of mitochondria, ER, and Golgi apparatus. These observations support further investigation of how treatment-associated changes across multiple organelles contribute to impaired tumor-cell function. The spatial mapping of FA-Au-Ag NMW-organelle interactions further supports rational nanostructure design for optimized subcellular targeting. Collectively, these results associate light-activated FA-Au-Ag NMW treatment with altered organelle morphology and cellular injury, providing a basis for investigating downstream molecular pathways (Figures 4, 5, and 6).

Transcriptomic profiling and molecular validation of cell death pathways induced by alloy nanostructures

To dissect the molecular mechanisms underlying photon-driven FA-Au-Ag NMW-induced tumor cell death, Figure 5 employs RNA sequencing (RNA-seq), KEGG/GO enrichment analyses, and western blot (WB)/qPCR validation, linking organelle dysfunction (Figure 4) to specific gene regulatory networks. These transcriptomic and proteomic analyses identify key signaling pathways and molecular targets, advancing our understanding of the multifaceted therapeutic effects of FA-Au-Ag NMWs in A2780 cells. A gene expression heatmap (Figure 5A) revealed distinct expression patterns of apoptosis, paraptosis, and autophagy-related genes across experimental groups, confirming the involvement of multiple cell death pathways in FA-Au-Ag NMW-mediated therapy—consistent with Figure 4's organelle disruption data. This transcriptomic signature reflects the coordinated response to NMW-induced plasmonic stress and organelle dysfunction, highlighting the complexity of the therapeutic mechanism beyond single-pathway apoptosis.

Therein, KEGG pathway enrichment analyses (Figures 5B–5E) were performed across four experimental comparisons to pinpoint pathway-specific activation: FA-Au-Ag NMW + LED vs. untreated, FA-Au-Ag NMW + LED vs. FA-Au-Ag NMW-only, NMW + LED vs. LED-only, and low- vs. high-concentration FA-Au-Ag NMW + LED. From the KEGG enrichment analysis, it can be seen that compared with other control groups, the FA-Au-Ag NMW + LED group has a significant enrichment of pathways related to high-stability paraptosis (brown box), mitochondrial autophagy (blue box), and autophagy (red box). Key apoptotic pathways were significantly enriched in the FA-Au-Ag NMW + LED group relative to all controls, with enrichment levels positively correlated with FA-Au-Ag NMW concentration. These results confirm that the synergistic effect of FA-Au-Ag NMWs and photon irradiation specifically activates apoptotic signaling, rather than non-specific cellular stress responses induced by FA-Au-Ag NMWs or irradiation alone.

GO enrichment analyses (Figures 5F–5J) further delineated intracellular processes linked to cell death. Cellular autophagy (Figure 5F) and ER-mitochondria-Golgi crosstalk (Figure 5G) were prominently enriched, aligning with Figure 4's observation of organelle dysfunction. Specific processes associated with mitochondria, ER, and Golgi apparatus (Figures 5H–5J) were dysregulated in the experimental group, confirming that NMW-induced organelle damage disrupts inter-organelle communication—a critical driver of cell death. Based on integrated heatmap, KEGG, and GO data, key photonic-induced gene expression factors are concentrated in the heat shock protein (HSP) family, which includes the HSP family that inhibits cell apoptosis caused by photothermal effects, and ER-mitochondria-Golgi crosstalk-related genes (GRP78: high expression of GRP78 enhances UPR and autophagy; TFRC: high expression of TFRC enhances iron uptake and inhibits paraptosis; TMED10: regulation of protein transport in the ER-Golgi apparatus secretion pathway, γ-secretase activity, and autophagy; SEC62: high expression of SEC62 will trigger excessive ER autophagy; CANX: high expression of CANX regulates the UPR pathway and alleviates ER stress) (Figure 5L) were identified, providing actionable molecular targets for mechanism optimization. WB and qPCR

(D and E) Fluorescent labeling of mitochondria, ER, and Golgi apparatus under irradiation alone (D) and combined FA-Au-Ag NMW plus irradiation (E).
(F–F4) 4D live-cell imaging tracks dynamic changes of three organelles within 0–60 min at 2 min intervals (Videos S3 and S4).
(G–G4) To examine the spatial relationships between FA-Au-Ag NMWs and intracellular structures, serial FIB-SEM images were analyzed using deep learning-assisted segmentation.
(H–H4) In this workflow, a U-Net model trained on annotated sections was used to assign predefined structural labels to image regions, and the resulting probability maps were converted into binary masks for 3D reconstruction, as detailed in the methods.
Quantitative summary data are presented as mean ± SD. Scale bars, 50 μm (A and B). See also Figures S27, S38, and S41; Table S1; and Videos S2, S3, and S4.

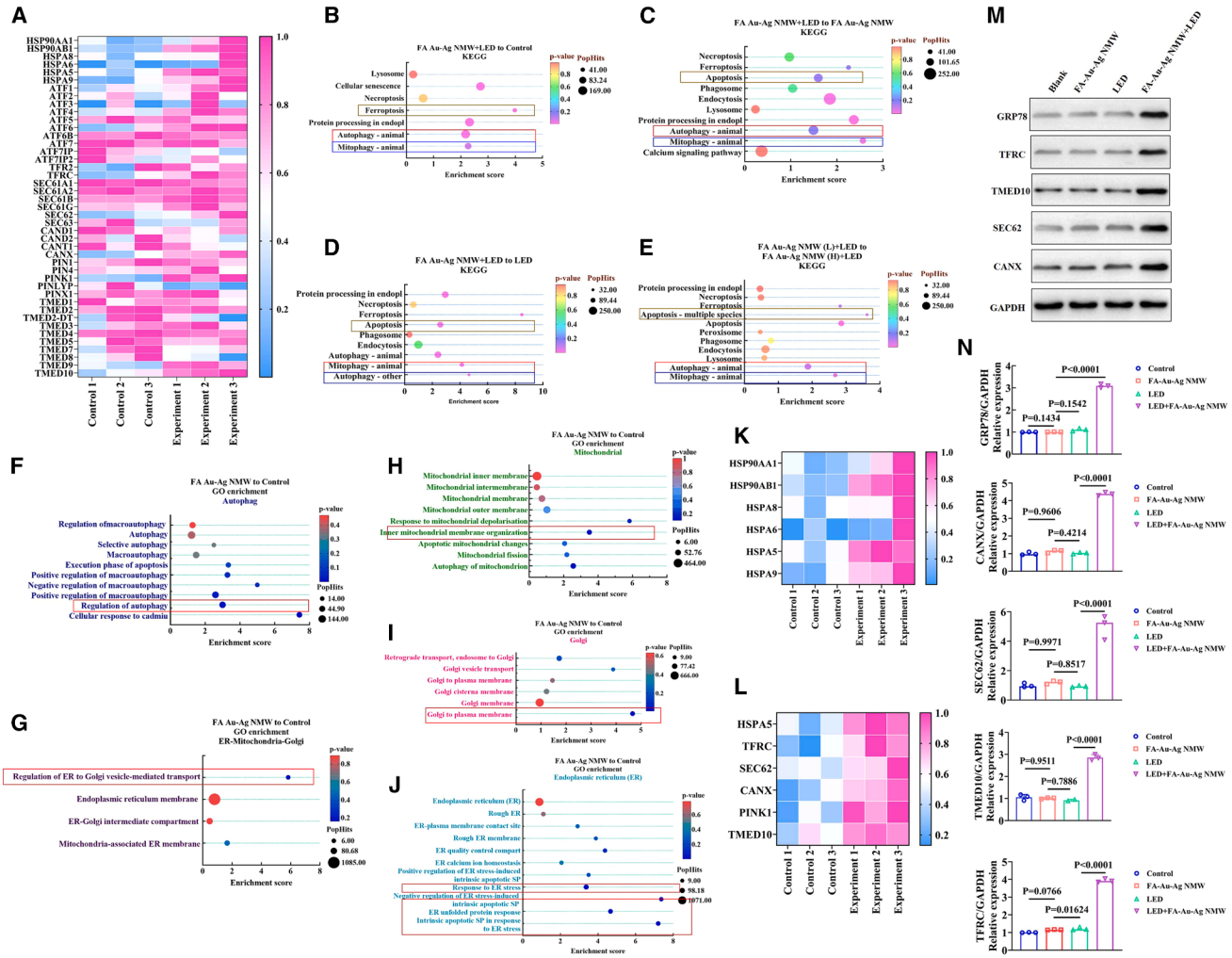


Figure 5. Transcriptomic screening and molecular validation of photon-triggered signaling pathways

(A) Heatmap of apoptosis-, paraptosis-, and autophagy-related genes.

(B–E) KEGG pathway enrichment across distinct control and treatment groups.

(F–J) GO enrichment analyses focusing on autophagy and ER-mitochondria-Golgi crosstalk.

(K and L) Screening of core photon-responsive genes involved in multi-organelle interaction.

(M and N) WB and qPCR validation of key genes regulating ER-mitochondria-Golgi signaling (n = 3 biological replicates). Quantitative qPCR data in (N) are presented as mean ± SD. See also Table S2.

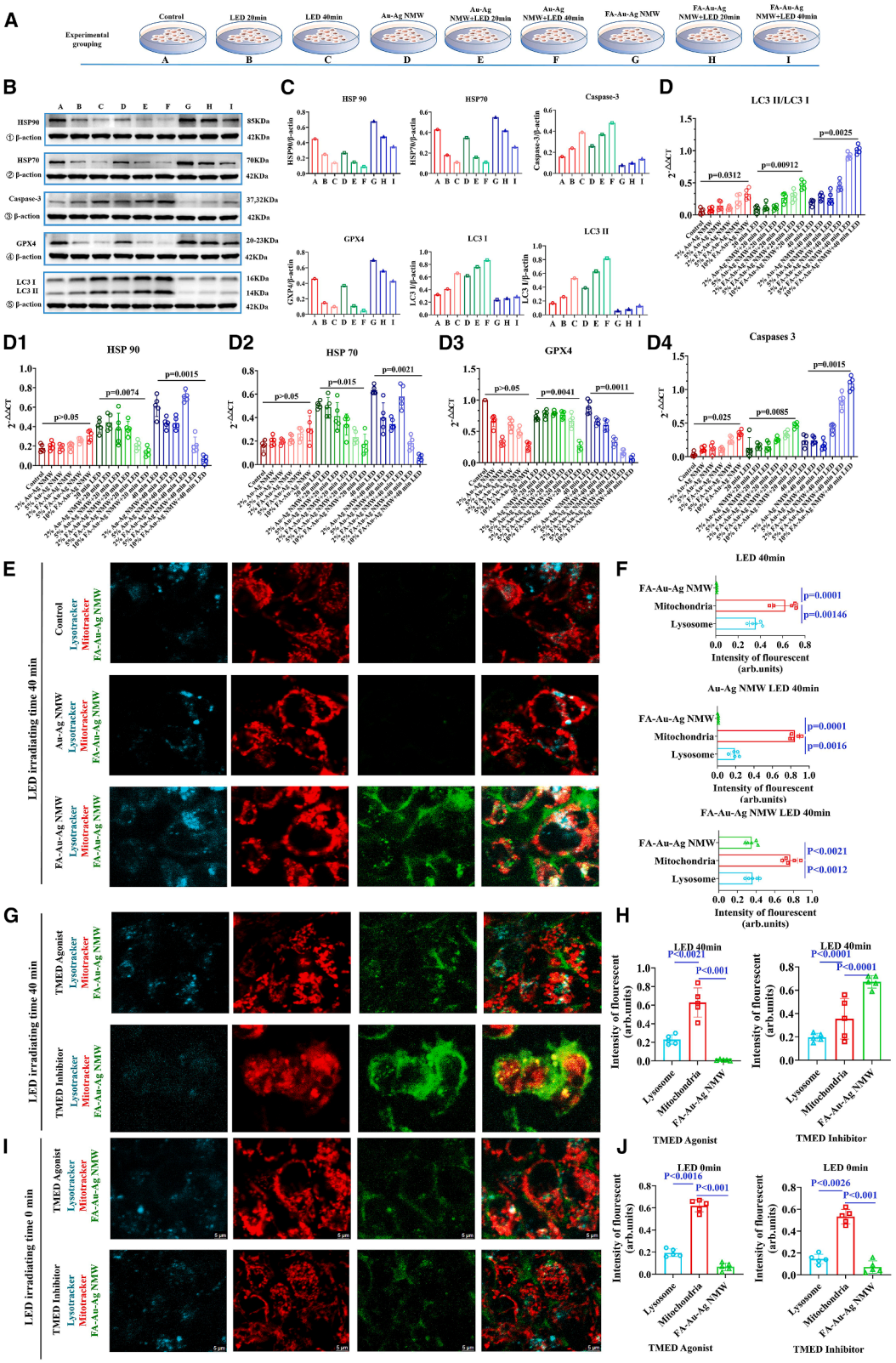
analyses (Figures 5M and 5N) validated the expression of key genes involved in ER-mitochondria-Golgi crosstalk, confirming transcriptomic findings at both protein and mRNA levels. Significant dysregulation of these genes was observed in the FA-Au-Ag NMW + LED group compared to controls, with three biological replicates ensuring statistical reliability (p values shown). This multi-layered validation (transcriptomic and proteomic) confirms that FA-Au-Ag NMWs regulate cell death by disrupting inter-organelle crosstalk, bridging molecular signaling to the organelle dysfunction observed in Figure 4.

Figure 5 findings integrate with prior data to establish a hierarchical therapeutic mechanism: FA-Au-Ag NMWs (Figure 1) leverage targeting and plasmonic properties (Figure 2) to induce organelle dysfunction (Figure 5), which in turn disrupts ER-mitochondria-Golgi crosstalk and activates apoptosis, paraptosis, and autophagy via specific gene regulatory networks. The identification of key molecular targets and pathways addresses the gap between phenotypic organelle damage and underlying molecular events. By activating multiple cell death pathways, FA-Au-Ag NMWs enhance therapeutic efficacy and reduce resistance risk. Collectively, these results solidify the molecular basis of NMW-mediated therapy, laying the groundwork for investigating HSP regulation and paraptosis contributions.

HSP-mediated regulation of organelle autophagy and paraptosis in tumor cells

HSPs are critical regulators of cellular stress responses and organelle homeostasis, while autophagy and paraptosis are key cell death pathways intertwined with organelle dysfunction. Figure 6 employs WB, qPCR, and LSCM to dissect the regulatory

CellPress
OPEN ACCESS



(legend on next page)

role of HSP70/HSP90 in FA-Au-Ag NMW-induced autophagy, paraptosis, and apoptosis, linking molecular signaling (Figure 5) to cellular phenotypic responses and refining the therapeutic mechanism in A2780 cells.

Nine *in vitro* cell groups were designed to clarify the synergistic effects of FA-Au-Ag NMWs, photon irradiation, and HSP modulation (Figure 6A), covering control, FA-Au-Ag NMW/irradiation-only, and HSP inhibitor/agonist combined treatment groups. WB analysis (Figure 6B) and quantitative protein expression profiling (Figure 6C) revealed distinct alterations in HSP90, HSP70, and key cell death-related proteins: Caspase-3 (apoptosis marker), GPX4 (paraptosis marker), and LC3I/LCII (autophagy marker). HSP90 and HSP70 were upregulated under photon-driven FA-Au-Ag NMW treatment, concurrent with Caspase-3 activation, GPX4 downregulation, and increased LC3II/LC3I ratio, confirming coordinated activation of apoptosis, paraptosis, and autophagy, which was further modulated by HSP inhibitors/agonists (see section V of the supplemental information).

The qPCR analysis (Figures 6D-d4) quantified transcriptional levels of HSP70, HSP90, and key cell death genes across diverse experimental groups (varying FA-Au-Ag NMW concentrations, irradiation durations, and NMW-irradiation combinations). Consistent with WB results, photon-driven FA-Au-Ag NMW treatment induced dose- and time-dependent upregulation of HSP70/HSP90 and Caspase-3, downregulation of GPX4, and increased LC3I/LCII expression-validating HSP involvement in transcriptional regulation of NMW-mediated cell death pathways. These findings align with Figure 5 transcriptomic data, reinforcing the role of HSPs in ER-mitochondria-Golgi crosstalk disruption.

LSCM imaging and fluorescence quantification (Figures 6E–6J) visualized mitochondria (red), lysosomes (cyan), and FA-Au-Ag NMWs (green) across treatment groups (five regions per sample for statistical rigor). After 40 min LED irradiation, FA-Au-Ag NMW-treated cells exhibited marked mitochondrial fragmentation and enhanced FA-Au-Ag NMW-lysosome co-localization versus controls and unfunctionalized FA-Au-Ag NMW groups (Figures 6E and 6F). TMED inhibitor/agonist treatment (Figures 6G–6J) modulated these effects: agonists exacerbated mitochondrial damage and FA-Au-Ag NMW-lysosome co-localization under irradiation, while inhibitors attenuated them, with no significant impact in non-irradiated groups-confirming photon-dependent HSP/TMED regulation of organelle dysfunction and FA-Au-Ag NMW intracellular trafficking.

Figure 6 solidifies HSP70/HSP90 as central regulators of FA-Au-Ag NMW-mediated therapy, linking their modulation to coordinated activation of apoptosis, paraptosis, and mitochondria-ER-Golgi autophagy. The dose- and time-dependent transcriptional/translational responses, coupled with HSP/TMED-dependent organelle dynamics, demonstrate the therapy's tunability—critical for clinical translation. These findings integrate with prior data to complete the mechanism: FA-targeted, photon-activated NMWs induce HSP upregulation, driving organelle autophagy and multi-pathway cell death. This tunable regulatory axis distinguishes FA-Au-Ag NMWs from conventional nanotherapeutics, offering strategies to optimize efficacy while minimizing off-target effects, and lays the groundwork for final validation of paraptosis contributions.

Paraptosis validation and HSP modulation with tumor-specific uptake of alloy nanostructures

Paraptosis is a key iron-dependent cell death pathway intertwined with HSP regulation and organelle dysfunction, while tumor-specific internalization is critical for reducing off-target toxicity. Figure 7 employs paraptosis inhibition assays, LSCM fluorescence co-localization, and inductively coupled plasma mass spectrometry (ICP-MS) to confirm paraptosis contributions, validate HSP modulation effects, and quantify NMW internalization, completing the mechanistic characterization of FA-Au-Ag NMWs in A2780 ovarian cancer therapy.

LSCM imaging clarified apoptotic phenotypes and HSP-dependent cell death regulation. Apoptotic cells (Figure 7A) exhibited characteristic morphological changes, including nuclear condensation and membrane blebbing, consistent with prior caspase activation data (Figure 6). Intracellular morphology post-apoptosis (Figure 7B) further revealed extensive organelle disruption, aligning with Figure 4's organelle dysfunction observations. HSP inhibitor (Figure 7C) and agonist (Figure 7D) treatments in FA-Au-Ag NMW + 20-min LED irradiation groups confirmed HSP modulation of cell death: HSP agonists exacerbated apoptotic and ferroptotic phenotypes, while inhibitors attenuated them-validating HSPs as tunable regulators of NMW-mediated multi-pathway cell death, consistent with Figure 6's findings. Competitive FA binding assays (Figure 7E) confirmed FOLR1-dependent FA-Au-Ag NMW internalization. Pre-incubation with excess free FA (20 min prior to treatment) significantly reduced FA-Au-Ag NMW accumulation in A2780 cells, as evidenced by diminished fluorescence signals. This result reinforces Figure 2's FOLR1 targeting validation, confirming that FA conjugation enables specific tumor cell recognition and internalization—critical for minimizing off-target effects in normal tissues.

Paraptosis inhibition assays combined with ROS detection (Figure 7F) confirmed paraptosis as a key cell death pathway. Fluorescence imaging (red: paraptosis; green: ROS) showed robust ferroptotic signals and ROS accumulation in FA-Au-Ag NMW + LED irradiation groups, while paraptosis inhibitor treatment significantly abrogated these signals. LSCM images, groups 1 (untreated), 2 (LED irradiation alone), 3 (FA-Au-Ag

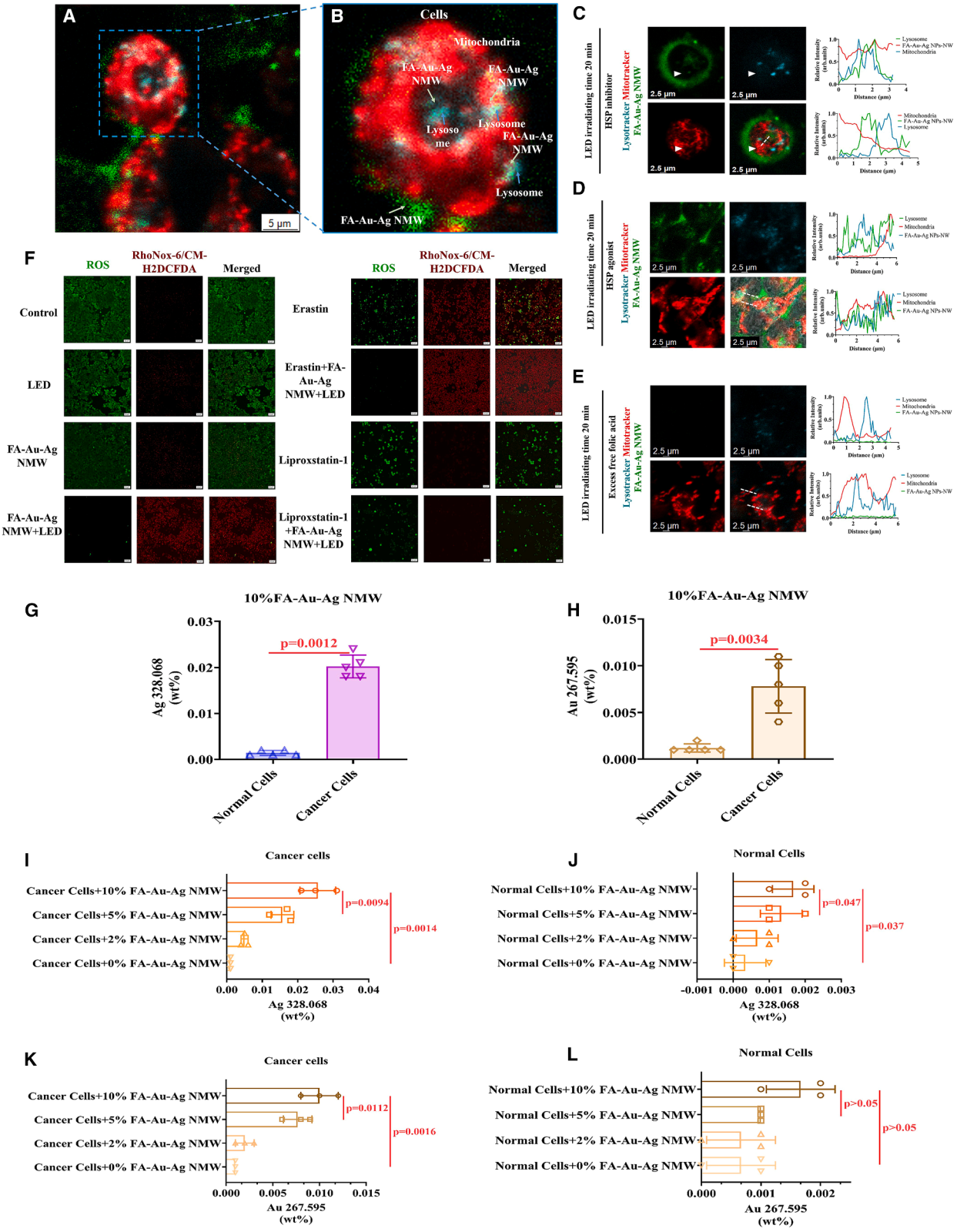
Figure 6. Molecular validation and pharmacological inhibition assays of paraptosis-related signaling *in vitro*

(A) Schematic of *in vitro* experimental grouping.

(B and C) WB detection of HSP70/HSP90 and apoptosis-related proteins under HSP agonist/inhibitor intervention.

(D–D4) qPCR quantification of core genes under varying nanomaterial concentrations and irradiation durations.

(E–J) LSCM observation and fluorescence quantification of mitochondria, lysosomes, and FA-Au-Ag NMW distribution upon TMED/HSP regulator treatment, with or without irradiation. Statistical analysis was performed with five detection regions per sample. Quantitative summary data are presented as mean ± SD. Scale bars, 5 μm (I). See also Figure S18.



(legend on next page)

NMW alone), and 7 (liproxstatin-1 alone) exhibited extensive green fluorescence (indicating ROS accumulation) with intact cell morphology, whereas no obvious deep red fluorescence (indicating paraptosis) was detected. In contrast, group 5 (erastin alone) showed complete disappearance of green fluorescence (ROS) accompanied by extensive deep red fluorescence (paraptosis), demonstrating that the paraptosis agonist erastin activates the paraptosis pathway and consequently induces cell inactivation. Notably, the results of group 7 (liproxstatin-1 alone) were completely opposite to those of group 5.

Based on the above results and control experiments, the data obtained from groups 4 (FA-Au-Ag NMW + LED), 6 (erastin + FA-Au-Ag NMW + LED), and 8 (liproxstatin-1 + FA-Au-Ag NMW + LED) revealed that FA-Au-Ag NMW combined with LED irradiation promotes cellular paraptosis. Specifically, the addition of erastin significantly enhanced the cell apoptotic rate, whereas the administration of liproxstatin-1 led to a decrease in the apoptotic rate. However, compared with group 4 (FA-Au-Ag NMW + LED alone), the total cell number in group 8 (liproxstatin-1 + FA-Au-Ag NMW + LED) was reduced. This phenomenon may be attributed to the potential pro-apoptotic effect of liproxstatin-1, which warrants further investigation in our subsequent studies. This confirms that NMW-mediated cell death relies on paraptosis activation, which is closely linked to ROS generation—likely derived from LSPR-driven photothermal effects and organelle dysfunction (Figures 2 and 3). These findings complement Figure 6's GPX4 downregulation data, solidifying paraptosis as a core component of the multi-pathway therapeutic mechanism.

ICP-MS analysis (Figures 7G–7L) quantified FA-Au-Ag NMW internalization by measuring intracellular Au and Ag contents. The Au and Ag contents in both cell types exhibited a concentration-dependent increase within the incubation period of 0%–10% FA-Au-Ag NPs-NW, and the accumulation levels in cancer cells were significantly higher than those in normal cells at each concentration point. Specifically, after 24 h of FA-Au-Ag NPs-NW exposure (at a concentration of 10% FA-Au-Ag NMW), the Au content in A2780 cancer cells reached 0.012 ± 0.005 [wt %]/10^6 cells, which was nearly 6-fold higher than that in normal cells (0.001 ± 0.0005 [wt %]/10^6 cells). Correspondingly, the Ag content in A2780 cells was 0.025 ± 0.005 [wt %]/10^6 cells, approximately nearly 12-fold higher than the value in normal cells (0.001 ± 0.0005 [wt %]/10^6 cells). Statistical analysis via independent samples *t* test confirmed that the differences in both Au and Ag accumulation between the two cell types were statistically significant ($p < 0.01$ for both Au and Ag). In contrast, negligible Au and Ag signals were detected in the negative control groups (cells without FA-Au-Ag NPs-NW treatment) and blank control groups (medium only), indicating that the measured signals were specifically derived from the internalized FA-Au-Ag NPs-NW rather than reagent background or intrinsic metal elements in cells. Intracellular Ag (Figure 7G) and Au (Figure 7H) levels correlated with NMW treatment, confirming efficient internalization. Tumor cells (Figures 7I and K) exhibited significantly higher Au/Ag accumulation than normal cells (Figures 7J and L) across different NMW concentrations, validating tumor-specific internalization—attributed to FOLR1 overexpression in A2780 cells. This quantitative data support the "double-selectivity" (FA targeting + photon activation) mechanism, confirming that NMWs preferentially accumulate in tumor cells, minimizing off-target toxicity.

Figure 7 completes the mechanistic characterization of FA-Au-Ag NMWs: FA-FOLR1 interaction enables tumor-specific internalization (validated by ICP-MS and competitive binding), photon activation triggers LSPR-driven ROS generation and HSP upregulation, which coordinate paraptosis, apoptosis, and organelle autophagy. Paraptosis inhibition assays confirm its non-redundant role in cell death, while HSP modulation offers a tunable strategy to optimize efficacy. Furthermore, several complementary strategies have been explored to overcome therapeutic resistance, including the induction of immunogenic cell death (ICD) and the inhibition of the DNA damage response (DDR). Whereas these approaches primarily exploit antitumor immunity or impaired genomic repair, respectively, the multi-organelle destructive pattern demonstrated here acts at the subcellular systems level by concurrently perturbing multiple organelles involved in cellular homeostasis. Such distributed organelle injury may restrict organelle-specific compensatory adaptation and thereby provide a potential advantage over strategies centered on a single intracellular target. From a combinatorial perspective, FA-Au-Ag NMW-mediated therapy could potentially be integrated with immune checkpoint blockade if bona fide ICD is demonstrated, or with DDR inhibitors if DNA damage or replication stress is found to contribute to the therapeutic response. These possibilities warrant further investigation.

Herein, a photon-assisted therapeutic platform based on multifunctional self-assembled FA-Au-Ag alloy nanomushroom-nanowires mediates tumor cell membrane disruption, intracellular translocation, multi-organelle autophagy/paraptosis induction, and subsequent tumor cell apoptosis. The core advantages of these nanostructures lie in their dual functionalities: tumor-targeted adhesion and photon-triggered enhanced LSPR at the membrane-binding sites (inducing membrane rupture and cytosolic entry), as well as photon-activated fluorescence emission that enables real-time localization and tracing. In a supplementary *in vivo* experiment, FA-Au-Ag NMWs were administered by intratumoral injection in mice bearing superficial tumors, followed by local light irradiation of the tumor region (section XIV; Figure S40). The preliminary observations are limited to the tested local treatment setting and do not establish systemic tumor targeting or clinical feasibility. More extensive *in vivo* evaluation and investigation of translational potential are planned for future

Figure 7. Paraptosis inhibition, fluorescence co-localization, and cellular internalization of FA-Au-Ag NMW

(A and B) LSCM imaging of apoptotic cellular morphology.

(C and D) Fluorescence co-localization analysis under HSP inhibitor and agonist intervention upon FA-Au-Ag NMW plus LED irradiation.

(E) Co-localization assay with excess free FA pre-treatment.

(F) Fluorescence imaging of paraptosis and ROS levels in different groups.

(G–L) ICP-MS quantification of intracellular Au and Ag contents to evaluate FA-Au-Ag NMW internalization in normal and tumor cells at varied concentrations ($n = 3$). Quantitative summary data are presented as mean ± SD. Scale bars: 5 μm in (A), 2.5 μm in (C–E), and 50 μm in (F). See also Figures S28 and S39.

studies. The proposed nanomaterial demonstrates potential in both fluorescence tracking and photothermal therapy, which could have promising implications in the field of nanomedicine.

METHODS

Additional experimental procedures are provided in supplemental methods. Supporting data are presented in Figures S1–S41 and Tables S1 and S2.

Materials

The human ovarian cancer cell A2780 (RRID: CVCL_0134) were obtained from Shanghai Zhongqiao Xinzhou Biotechnology Co. Ltd. (Shanghai, China). Cells were cultured in RPMI 1640 medium (ATCC modification, Gibco, Thermo Fisher, USA) supplemented with 10% fetal bovine serum (FBS, Hyclone, Thermo Fisher, USA), 2 mM glutamine (Corning, USA), and 1% penicillin/streptomycin (Corning, USA) at 37°C in a humidified atmosphere at 5% CO2. PBS: phosphate-buffered saline w/o calcium w/o magnesium, 500 mL/bottle. Culture medium: DMEM high glucose w/L-glutamine w/sodium pyruvate, 500 mL/bottle, fetal bovine serum (FBS): Australia, USDA approved/extra fetal bovine serum, 500 mL/bottle, antibiotic: antibiotic-antimycotic 100×, 100 mL/bottle; complete culture solution: prepared by adding 10% fetal bovine serum and 1% antibiotics to DMEM by volume. KGI Cell Viability Assay Kit (CalceinAM and PI method, specifications 1000 tests, full name: Live & Dead Viability/Cytotoxicity Assay Kit for Animal Cells; Calcein AM: Ex/Em: 495 nm/520 nm) (PI: Ex/Em: 530 nm/620 nm). Gold mesh (Quantifoil, R 1.2/1.3, 300 mesh Au) was employed for EM. LysoTracker red (C1046, 1 mM, 50 μL) was used as a red-fluorescent lysosomal probe capable of permeating cell membranes for selective staining of lysosomes in live cells. Mito-Tracker Deep Red FM (C1032, 50 μg) was used as a cell-permeable deep-red fluorescent mitochondrial probe, which specifically labels biologically active mitochondria and allows detection of mitochondrial membrane potential in live cells.

Cell culture incubator: Qingdao Haier Biomedical Technology Company, Haier CO_2, incubator, HCP-168E, 95 W. LED light: bull, 30 W; yee LED light, 10.8 W. Zeiss cryo-electron microscope working temperature: −165°C. Ultra-high resolution multi-photon laser confocal microscope for live cells (instrument model: TCS SP8 STED 3×, laboratory: W251, Translational Medicine Building, Minhang Campus, Shanghai Jiao Tong University). High-resolution laser confocal microscope (instrument model: Leica STELLARIS 5, laboratory: W250, Translational Medicine Building, Minhang Campus, Shanghai Jiao Tong University) (both instruments employed for cellular-level imaging and data acquisition follow similar operating procedures and display results).

4D live-cell spatiotemporal imaging of organelle dynamics

To investigate the localized impact of Au-Ag nanomushrooms on cellular organelles under light irradiation, real-time multi-channel fluorescence imaging was performed. This approach aimed to characterize the morphological perturbations and spatial redistribution of the ER, mitochondria, and Golgi apparatus in response to the nanomaterial-mediated effects. By establishing a dynamic evaluation framework, we sought to capture the cascade of structural transformations triggered by the activation of the nanomushrooms within the intracellular environment.

Instrumentation: ZEISS LSM 990

Live-cell imaging was conducted using the ZEISS LSM 990 laser scanning confocal microscope (Carl Zeiss Microscopy GmbH, Germany). The system is equipped with high-sensitivity GaAsP (gallium arsenide phosphide) detectors and the Airyscan 2 module, which provides super-resolution capabilities and high signal-to-noise ratios while minimizing phototoxicity during extended observations. An integrated environmental chamber was utilized to maintain stable physiological conditions (37°C, 5% CO_2) throughout the duration of the experiments.

Organelle-specific fluorescent probes

A triple-staining protocol was implemented to simultaneously track the dynamics of multiple organelles in living cells:

ER: labeled with ER-Tracker Blue-White DPX (Thermo Fisher, MX4351-50UL), a probe that specifically binds to the ER membrane.

Golgi apparatus: visualized using Golgi-Tracker Red (BODIPY TR Ceramide) (MX4355-1MG), which targets the lipid-rich structures of the Golgi complex.

Mitochondria: identified with MitoTracker Deep Red FM (Invitrogen, M22426), a carbocyanine-based dye that localizes to the mitochondrial matrix.

Laser-induced activation and time-lapse acquisition

A2780 cells, previously treated with Au-Ag nanomushrooms, were seeded in glass-bottom dishes and stained according to the manufacturers' protocols. To trigger the nanomaterial-mediated effects, the cells were subjected to *in situ* irradiation using the internal 488 nm laser line of the confocal microscope at 10% power intensity. Sequential scanning was employed across the three fluorescence channels to eliminate spectral crosstalk. Time-lapse images were acquired at 2-min intervals over a total period of 64 min, yielding a sequence of 32 image groups. This temporal resolution enabled high-resolution monitoring of the structural evolution of the organelle networks, capturing the progression from initial nanomaterial activation to the subsequent manifestations of cellular stress.

Serial FIB-SEM tomography

Volumetric data acquisition setup high-resolution 3D ultrastructural characterization of LED-irradiated A2780 cells containing Au-Ag nanomushrooms was performed using a ZEISS Crossbeam 550 FIB-SEM. The system is equipped with a Gemini II electron optical column, which provides high-resolution imaging and exceptional contrast at low accelerating voltages. The automated serial sectioning and imaging ("slice-and-view") workflow was managed by the Atlas 5 3D tomography software module. This software facilitates high-throughput 3D analysis by precisely coordinating the ion milling and electron imaging cycles while maintaining consistent slice thickness through automated tracking and focus algorithms.

Instrument introduction The ZEISS Crossbeam 550 is a high-throughput FIB-SEM platform designed for advanced 3D analysis and precision sample preparation. This system integrates the Gemini II field-emission scanning electron microscope (FE-SEM) optics with the ion-sculptor FIB column, combining

powerful imaging performance with superior processing capabilities. The Gemini II column features a dual condenser system that ensures high-resolution imaging and exceptional contrast at both low accelerating voltages and high beam currents. Simultaneously, the ion-sculptor FIB facilitates accurate material removal with minimal sample damage and reduced amorphization, operating across a wide beam current range from 1 pA to 100 nA. Supported by the Atlas 5 software suite, the system enables automated 3D tomography with consistent slice thickness and reliable volumetric tracking, making it a robust tool for characterizing complex biological architectures.

Ion milling and SEM imaging parameters precise material removal was executed using the ion-sculptor FIB column, operating at an accelerating voltage of 30 kV. This column is specifically designed to minimize amorphous damage to sensitive biological samples while maintaining high resolution. Following the excavation of a trench to expose the region of interest, the ion beam generated serial sections with a Z-step size of 10 nm. The newly exposed block-face was imaged after each milling step using a low landing energy (1.5–2.0 kV) to maximize surface sensitivity and suppress charging effects in the resin-embedded cells.

Signal detection and data acquisition to simultaneously resolve cellular morphology and nanomaterial distribution, dual Inlens detectors were utilized. The Inlens SE detector was optimized to capture high-resolution ultrastructural details of cellular organelles. Concurrently, the Inlens EsB (energy-selective backscattered) detector was employed to provide high-purity compositional contrast. By applying a specific filtering grid voltage, the Au-Ag nanomushrooms were clearly distinguished from the organic cellular matrix based on their higher atomic number. For two distinct treated A2780 cell samples, continuous stacks of 1,409 and 933 images were acquired, respectively, providing a comprehensive volumetric dataset for 3D reconstruction and analysis.

3D reconstruction of cellular structures

To elucidate the intricate spatial relationships between the Au-Ag nanomushrooms and the intracellular environment, a high-resolution 3D volumetric reconstruction was performed. By leveraging a large-scale dataset of serial EM sections, we integrated deep learning-based computational analysis with advanced rendering techniques. This workflow facilitated the transition from two-dimensional ultrastructural observations to a comprehensive 3D architectural model, providing a robust framework for assessing the structural impacts and spatial perturbations of intracellular organelles under the influence of the Au-Ag nanomushrooms.

Image pre-processing and alignment

The volumetric analysis was conducted within the ZEISS arivis Pro v.4.4.0 software environment (Carl Zeiss Microscopy GmbH, Germany). The raw dataset, comprising 1,409 serial EM sections, first underwent a global alignment process to ensure spatial continuity along the z axis. This was achieved through translation and rigid registration algorithms, which corrected for mechanical shifts and minor deformations inherent in the serial sectioning process. The resulting registered image stack provided a spatially coherent 3D volume, serving as the foundational framework for subsequent semantic segmentation and structural analysis.

Deep learning-based segmentation

For the identification of complex intracellular structures, a deep learning-based segmentation approach was implemented using the arivis AI deep learning trainer module. The target structures were classified into seven categories: Au-Ag nanomushrooms, lipid droplets, ER, mitochondria, cell membranes, the nucleus, and the background. To develop a robust training dataset, nine representative slices were selected from the 1,409-image stack and annotated using the AI-assisted mode to establish high-fidelity ground truth. A UNet convolutional neural network architecture was employed for model training, which was executed for 350 epochs on a high-performance computational workstation. The hardware configuration included an AMD Ryzen Threadripper PRO 5995WX 64-core CPU, 512 GB of RAM, and an NVIDIA GeForce RTX 4090 GPU. The final trained model achieved a mean intersection over union (IoU) of 96% on the training set. Automated volumetric inference was subsequently performed on the entire image stack using the deep learning segmenter module within the analysis pipeline, generating semantic probability maps that were converted into binary masks.

3D reconstruction and visualization

The validated binary masks were integrated into the arivis analysis pipeline for 3D reconstruction. Surface rendering was applied to each categorized organelle and the Au-Ag nanomushrooms to facilitate the visualization of their spatial distribution and relative orientations within the cell. The entire volumetric model was rendered using a high-performance 3D engine, enabling a detailed exploration of the structural interactions and physical contact points between the nanomaterials and the intracellular components. From these reconstructed 3D objects, quantitative morphometric parameters—including volume, surface area, and spatial coordinates—were extracted to support the subsequent analysis of how the Au-Ag nanomushrooms influence cellular architecture and organelle integrity.

neaSNOM testing

Instrument description

Near-field measurements were conducted using a scattering-type scanning near-field optical microscope (neaSNOM, Neaspec GmbH, Germany). The system integrates a metal-coated AFM probe (Pt/Ir-coated Si, apex radius ~20–30 nm) with interferometric pseudo-heterodyne detection, enabling background-free amplitude and phase imaging with ~20 nm spatial resolution. The AFM tip operated in tapping mode (~250 kHz) and near-field signals were demodulated at higher harmonics ($n \geq 2$) to isolate the genuine near-field component. Monochromatic excitation at 950 and 980 nm was used to drive localized plasmonic responses in the hybrid nanostructures.

Sample preparation

Au-Ag NPs-NW hybrids were dispersed in deionized water and briefly sonicated (30 s). A 10 μL aliquot was drop-cast onto cleaned Si substrates and dried under ambient conditions immediately before imaging.

Near-field optical measurements

During imaging, the illuminated AFM tip acted as a nanoscale optical antenna, producing tightly confined fields that couple to

plasmonic modes within the Au-Ag hybrid structures. Near-field amplitude and phase signals were recorded simultaneously with topography using the closed-loop scanner (50 μm × 50 μm lateral range; <0.2 nm RMS vertical noise). Polarization and incidence angle were adjusted for optimal plasmonic coupling at both excitation wavelengths.

Data processing

Data were analyzed using Gwyddion (64-bit). Only line-profile analysis was performed on the near-field amplitude maps without additional filtering or reconstruction. Line sections across selected structural features revealed pronounced localized enhancements at the Au nanoparticle sites, consistent with excitation of surface plasmon resonances (SPRs) under both 950 and 980 nm illumination.

TEM

Aliquots of FA-Au-Ag NMW were ultrasonicated for ≥5 min. A 5-μL droplet of the suspension was deposited onto a carbon-coated copper grid and air dried. Morphological characterization was performed using a Thermo Fisher TALOS F200 × 200 kV TEM, followed by EDS elemental analysis and surface-mapping measurements.

XPS

XPS measurements were performed using a Thermo Scientific Nexsa G2 spectrometer equipped with a monochromated Al Kα X-ray source (1,486.6 eV). A 400-μm X-ray beam spot was selected for all measurements. Survey spectra were collected with a pass energy of 100 eV and a step size of 1.0 eV, while high-resolution spectra for individual elements were obtained using a pass energy of 50 eV and a step size of 0.05 eV. The incident X-ray beam was aligned at a 30° angle relative to the sample surface. A built-in charge neutralization system (flood gun) was applied during all acquisitions to minimize surface charging.

Prior to analysis, samples were dried under ambient conditions and fixed onto a conductive sample holder using double-sided carbon tape to ensure proper electrical grounding. All spectra were calibrated to the C 1s peak at 284.8 eV to correct for residual charging. Background subtraction was performed using a Shirley-type background, and peak deconvolution was carried out with mixed Gaussian-Lorentzian line shapes. Quantification of elemental composition was computed using atomic sensitivity factors provided by the instrument software.

FTIR spectroscopy

Fourier transform infrared spectroscopy (FTIR) measurements were performed using a Nicolet 6700 spectrometer (Thermo Fisher Scientific, USA). The instrument operates over a spectral range of 12,000–350 cm^{-1} with a resolution better than 0.09 cm^{-1}, wavenumber accuracy better than 0.01 cm^{-1}, and a signal-to-noise ratio exceeding 50,000:1. A DTGS room temperature detector was employed for all measurements.

Samples were analyzed using transmission and attenuated total reflectance (ATR) modes depending on the material form. The system is equipped with a Ge-crystal ATR module, variable-temperature and variable-angle transmission accessories (0°–90°), infrared polarization optics, and standard transmission components including pellet pressing tools and liquid cells. Spectra were collected using Omnic software, and raw data were exported as *.SPA or *.csv files for further analysis with Origin or Excel.

FTIR spectroscopy was used to identify functional groups, assess molecular structures, and analyze organic and inorganic components present in the samples. Measurements were performed on solid, liquid, or thin-film specimens as appropriate. All spectra were baseline-corrected and normalized prior to spectral analysis.

Photochemical treatment of ovarian cancer cells (A2780)

Preparation of Au-Ag nanoparticle-decorated silver nanowires (FA-Au-Ag NMW)

The nanowire stock solution was diluted 3-fold with PBS for all experiments (i.e., 1 mL of the original stock was diluted to 3 mL).

Cell-nanowire co-incubation

The diluted nanowire suspension was added to Petri dishes containing adherent A2780 cells and complete culture medium at a final concentration of 1% (10 μL/mL) or 2%, according to the experimental design. Typically, 10 mL of culture medium was used for a 10-cm dish, and 2 mL was used per well in a six-well plate.

Incubation

Cells were incubated for 2 h to ensure sufficient interaction between nanowires and the cell surface.

Removal of excess nanowires

After incubation, nanowire deposition at the bottom of the dish was confirmed using an inverted microscope. The medium was then aspirated, and cells were gently washed twice with PBS to remove unbound nanowires, followed by replenishment with fresh complete medium.

LED irradiation

The culture dishes were exposed to LED illumination. Irradiation duration was controlled according to the experimental gradient.

Live/dead staining for confocal microscopy

Calcein-AM and PI stock reagents were equilibrated to room temperature for 30 min. A working PI solution was prepared by adding 5 μL of a 16 mM PI stock to 10 mL of buffer, yielding an 8 μM PI solution. A Calcein-AM working solution was prepared by adding 5 μL of a 4 μM stock into 10 mL of the PI solution, followed by vortex mixing. The final live/dead staining solution was prepared fresh on the day of use due to hydrolysis sensitivity of Calcein-AM. Adherent cells were washed gently with PBS. An adequate volume of staining solution was added to fully cover the cell monolayer. Samples were incubated for 30–45 min at room temperature. The staining solution was removed, cells were washed with PBS, and samples were prepared for confocal imaging. A confocal microscope was pre-equipped with excitation/emission channels appropriate for Calcein-AM and PI fluorescence. Images were acquired and saved for further analysis.

Lysosome and mitochondria staining

LysoTracker red staining

LysoTracker red was diluted in cell culture medium or appropriate buffer (e.g., HBSS with Ca^{2+} and Mg^{2+}) to a final

concentration of 50–200 nM. The working solution was pre-warmed to 37°C before use. Adherent cells were incubated with the LysoTracker red solution at 37°C for 5–60 min. After incubation, cells were washed with fresh culture medium to remove unbound dye. Lysosomes were visualized using a fluorescence or confocal laser scanning microscope. Dye concentration and incubation time were optimized to minimize background fluorescence while maintaining effective lysosomal labeling.

Mito-Tracker deep red FM staining

Mito-Tracker deep red FM stock solution (200 μM) was prepared by dissolving 50 μg of powder in 460 μL anhydrous DMSO. The stock was diluted 1:5,000 in culture medium or suitable buffer to obtain a working concentration of 20–200 nM. The working solution was pre-warmed to 37°C. Adherent cells were incubated with Mito-Tracker deep red FM at 37°C for 15–30 min, followed by two washes with fresh pre-warmed medium. Fluorescence was observed using a fluorescence or confocal microscope. Dye concentration and incubation time were optimized to reduce non-specific staining and photobleaching.

Flow cytometry live/dead staining

Cells were harvested, centrifuged, and washed twice with PBS. A live/dead working solution was prepared following the same steps as in confocal staining, and then diluted 1:1,000 in PBS. A total of 200 μL of the diluted reagent was added to each cell pellet, resuspended, and incubated for 15–30 min at room temperature. Appropriate fluorescence channels were selected. Double-negative and single-stained controls were used to set voltage, compensation, and gate boundaries. A quadrant (cross-gate) strategy was applied to all samples. Flow rate was controlled to maintain approximately 1,000 events/s. Live/dead cell ratios were determined from quadrant distributions.

Virus infection and transient transfection assay

Cell seeding

A2780 ovarian cancer cells were seeded in culture dishes and grown to ~70% confluence under standard conditions.

Viral infection

Viral vectors carrying FOLR1(h)-siRNA or scramble control sequences were added to the cells in serum-free medium. Cells were incubated for 6–8 h to allow efficient viral entry.

Post-infection culture

After infection, the medium was replaced with complete culture medium, and cells were further cultured for 24–48 h to achieve transient knockdown of FRα.

Controls

Cells treated with scramble virus or without viral infection served as negative controls.

Cryo-EM

Before cell seeding, sterilized gold EM grids were placed at the bottom of culture dishes to allow cells to grow directly on the grids. Experimental and control samples underwent the photochemical treatment procedure described for A2780 cells. Cells were vitrified by high-pressure freezing. Localization was performed using CSEI-based methods. Cryo-EM imaging and cryo-ET data acquisition were conducted. Image processing was performed as described in supplemental methods. Motion analysis was carried out according to standard protocols.

WB analysis

A2780 cells were cultured in dishes and treated with FA-Au-Ag NMW. Experimental groups included cells with or without the HSP inhibitor (17-AAG) or HSP agonist (tamoxifen). Following LED irradiation for varying durations (according to experimental gradient), cells were washed with PBS and lysed using RIPA buffer supplemented with protease and phosphatase inhibitors. Cell lysates were collected and centrifuged at 12,000 × *g* for 10 min at 4°C to obtain supernatants. Protein concentrations were measured using the BCA assay. Equal amounts of protein were mixed with loading buffer, denatured at 95°C for 5 min, and resolved on SDS-PAGE gels. Proteins were then transferred onto PVDF membranes. Membranes were blocked with 5% non-fat milk in TBST for 1 h at room temperature, followed by incubation overnight at 4°C with primary antibodies against HSP70, HSP90, Caspase-3, GPX4, and LC3I/II. After washing, membranes were incubated with appropriate HRP-conjugated secondary antibodies for 1 h at room temperature. Protein bands were visualized using enhanced chemiluminescence (ECL) reagents and imaged with a chemiluminescence detection system. Band intensities were quantified using ImageJ software. Expression changes of HSP70, HSP90, Caspase-3, GPX4, and LC3I/II were analyzed relative to the loading control (β-actin). Statistical analysis was performed to compare the effects of FA-Au-Ag NMW treatment, LED irradiation duration, and HSP modulators.

Statistical analysis

All experimental data were presented as mean ± standard deviation (SD). Statistical comparisons between groups were performed using GraphPad Prism (v.6). *p* values calculated are indicated.

Data randomization statement

All of the data collection was randomized, and cell samples were randomly assigned to the various experimental groups. In addition, both experimental conditions and stimulus presentation were randomized. However, the researchers involved in data collection and analysis were not blinded to the experimental conditions. No data were excluded from the analysis.

RESOURCE AVAILABILITY

Lead contact

Further information and requests for resources and reagents should be directed to and will be fulfilled by the lead contact, Hailang Dai (hailangdai@sjtu.edu.cn).

Materials availability

Materials generated in this study are available from the lead contact upon request.

Data and code availability

- All data reported in this paper are available from the lead contact upon request.
- The original Java code developed for this study to generate the COMSOL simulation geometries is available on Zenodo at https://doi.org/10.5281/zenodo.23293160.

- Any additional information required to reanalyze the data reported in this paper is available from the lead contact upon request.

ACKNOWLEDGMENTS

This work was supported by the National Natural Science Foundation of China (NSFC) (12574361), the Shanghai Municipal Science and Technology Major Project (grant no. 2019SHZDZX01-06), and Natural Science Foundation of Shanghai (23ZR1428400).

AUTHOR CONTRIBUTIONS

H.Q. and H.D., writing – review and editing, visualization, and resources; H.D. and X.C., supervision and funding acquisition; Y.L. and Y.Q., software and resources; H.Q. and Y.Q., methodology and investigation; H.D., writing – original draft, project administration, formal analysis, data curation, and conceptualization; X.C., writing – review and editing, visualization, validation, supervision, and conceptualization. All authors have reviewed and approved the final version of the manuscript being submitted. We affirm that the article is our original work, has not been previously published, and is not under consideration for publication elsewhere.

DECLARATION OF INTERESTS

The authors declare that they have no known competing financial interests, commercial affiliations, personal relationships, or other potential conflicts of interest that could have influenced the work reported in this paper.

SUPPLEMENTAL INFORMATION

Supplementary data related to this article can be found online at https://doi.org/10.1016/j.xcrp.2026.103652

Received: May 17, 2026
Revised: August 24, 2026
Accepted: October 22, 2026

REFERENCES

1. Chen, Y., Li, X., Yang, M., and Liu, S.-B. (2024). Research progress on morphology and mechanism of programmed cell death. Cell Death Dis. *15*, 327. https://doi.org/10.1038/s41419-024-06712-8.
2. Hengartner, M.O. (2000). The biochemistry of apoptosis. Nature *407*, 770–776. https://doi.org/10.1038/35037710.
3. Zhang, S., Peng, X., Yang, S., Li, X., Huang, M., Wei, S., Liu, J., He, G., Zheng, H., Yang, L., et al. (2022). The regulation, function, and role of lipophagy, a form of selective autophagy, in metabolic disorders. Cell Death Dis. *13*, 132. https://doi.org/10.1038/s41419-022-04593-3.
4. Kagan, V.E., Mao, G., Qu, F., Angeli, J.P.F., Doll, S., Croix, C.S., Dar, H.H., Liu, B., Tyurin, V.A., Ritov, V.B., et al. (2017). Oxidized arachidonic and adrenic PEs navigate cells to ferroptosis. Nat. Chem. Biol. *13*, 81–90. https://doi.org/10.1038/nchembio.2238.
5. Mocarski, E.S., Upton, J.W., and Kaiser, W.J. (2011). Viral infection and the evolution of caspase 8-regulated apoptotic and necrotic death pathways. Nat. Rev. Immunol. *12*, 79–88. https://doi.org/10.1038/nri3131.
6. Potting, C., Tatsuta, T., König, T., Haag, M., Wai, T., Aaltonen, M.J., and Langer, T. (2013). TRIAP1/PRELI complexes prevent apoptosis by mediating intramitochondrial transport of phosphatidic acid. Cell Metab. *18*, 287–295. https://doi.org/10.1016/j.cmet.2013.07.008.
7. Fan, D., Cao, Y., Cao, M., Wang, Y., Cao, Y., and Gong, T. (2023). Nanomedicine in cancer therapy. Signal Transduct. Targeted Ther. *8*, 293. https://doi.org/10.1038/s41392-023-01536-y.
8. Nam, J., Son, S., Park, K.S., Zou, W., Shea, L.D., and Moon, J.J. (2019). Cancer nanomedicine for combination cancer immunotherapy. Nat. Rev. Mater. *4*, 398–414. https://doi.org/10.1038/s41578-019-0108-1.
9. Stockwell, B.R. (2022). Ferroptosis turns 10: Emerging mechanisms, physiological functions, and therapeutic applications. Cell *185*, 2401–2421. https://doi.org/10.1016/j.cell.2022.06.003.
10. Ryu, K.W., Fung, T.S., Baker, D.C., Saoi, M., Park, J., Febres-Aldana, C.A., Aly, R.G., Cui, R., Sharma, A., Fu, Y., et al. (2024). Cellular ATP demand creates metabolically distinct subpopulations of mitochondria. Nature *635*, 746–754. https://doi.org/10.1038/s41586-024-08146-w.
11. Spinelli, J.B., and Haigis, M.C. (2018). The multifaceted contributions of mitochondria to cellular metabolism. Nat. Cell Biol. *20*, 745–754. https://doi.org/10.1038/s41556-018-0124-1.
12. Zhu, J., Schwörer, S., Berisa, M., Kyung, Y.J., Ryu, K.W., Yi, J., Jiang, X., Cross, J.R., and Thompson, C.B. (2021). Mitochondrial NADP(H) generation is essential for proline biosynthesis. Science *372*, 968–972. https://doi.org/10.1126/science.abd5491.
13. Boehnke, N., Straehla, J.P., Safford, H.C., Kocak, M., Rees, M.G., Ronan, M., Rosenberg, D., Adelmann, C.H., Chivukula, R.R., Nabar, N., et al. (2022). Massively parallel pooled screening reveals genomic determinants of nanoparticle delivery. Science *377*, eabm5551. https://doi.org/10.1126/science.abm5551.
14. Dumitru, R., Gama, V., Fagan, B.M., Bower, J.J., Swahari, V., Pevny, L.H., and Deshmukh, M. (2012). Human embryonic stem cells have constitutively active Bax at the Golgi and are primed to undergo rapid apoptosis. Mol. Cell *46*, 573–583. https://doi.org/10.1016/j.molcel.2012.04.002.
15. Sassano, M.L., Tyurina, Y.Y., Diokmetzidou, A., Vervoort, E., Tyurin, V.A., More, S., La Rovere, R., Giordano, F., Bultynck, G., Pavie, B., et al. (2025). Endoplasmic reticulum–mitochondria contacts are prime hotspots of phospholipid peroxidation driving ferroptosis. Nat. Cell Biol. *27*, 902–917. https://doi.org/10.1038/s41556-025-01668-z.
16. Deretic, V. (2021). Autophagy in inflammation, infection, and immunometabolism. Immunity *54*, 437–453. https://doi.org/10.1016/j.immuni.2021.01.018.
17. Bukowski, K., Kciuk, M., and Kontek, R. (2020). Mechanisms of multidrug resistance in cancer chemotherapy. Int. J. Mol. Sci. *21*, 3233. https://doi.org/10.3390/ijms21093233.
18. de Lázaro, I., and Mooney, D.J. (2021). Obstacles and opportunities in a forward vision for cancer. Nat. Mater. *20*, 1469–1479. https://doi.org/10.1038/s41563-021-01047-7.
19. Peña, Q., Wang, A., Zaremba, O., Shi, Y., Scheeren, H.W., Metselaar, J.M., Kiessling, F., Pallares, R.M., Wuttke, S., and Lammers, T. (2022). Metallodrugs in cancer nanomedicine. Chem. Soc. Rev. *51*, 2544–2582. https://doi.org/10.1039/D1CS00468A.
20. Zhang, C., Yan, L., Wang, X., Zhu, S., Chen, C., Gu, Z., and Zhao, Y. (2020). Progress, challenges, and future of nanomedicine. Nano Today *35*, 101008. https://doi.org/10.1016/j.nantod.2020.101008.
21. Matus, M.F., and Häkkinen, H. (2023). Understanding ligand-protected noble metal nanoclusters at work. Nat. Rev. Mater. *8*, 372–389. https://doi.org/10.1038/s41578-023-00537-1.
22. Pearce, A.K., Wilks, T.R., Arno, M.C., and O'Reilly, R.K. (2021). Synthesis and applications of anisotropic nanoparticles with precisely defined dimensions. Nat. Rev. Chem *5*, 21–45. https://doi.org/10.1038/s41570-020-00232-7.
23. Baffou, G., Cichos, F., and Quidant, R. (2020). Applications and challenges of thermoplasmonics. Nat. Mater. *19*, 946–958. https://doi.org/10.1038/s41563-020-0740-6.
24. Cheong, J., Jo, A., Lee, J., Lee, S., Lee, J.-u., Lee, J.-H., Lee, H., and Cheon, J. (2024). Engineered nanoparticles for clinical assays. Nat. Rev. Bioeng. *2*, 887–905. https://doi.org/10.1038/s44222-024-00208-y.